2011

PRODUCTION OF BIOFUEL INTERMEDIATES FROM WOODY FEEDSTOCKS VIA FAST PYROLYSIS AND TORREFACTION

Jordan Lee Klinger
Michigan Technological University

Follow this and additional works at: https://digitalcommons.mtu.edu/etds

Part of the Chemical Engineering Commons

PRODUCTION OF BIOFUEL INTERMEDIATES FROM WOODY FEEDSTOCKS

VIA FAST PYROLYSIS AND TORREFACTION

By

Jordan Lee Klinger

A THESIS

Submitted in partial fulfillment of the requirements for the degree of

MASTER OF SCIENCE

(Chemical Engineering)

MICHIGAN TECHNOLOGICAL UNIVERSITY

2011

This thesis, "Production of Biofuel Intermediates from Woody Feedstocks via Fast Pyrolysis and Torrefaction," is hereby approved in partial fulfillment of the requirements for the Degree of MASTER OF SCIENCE IN CHEMICAL ENGINEERING.

Department of Chemical Engineering

Signatures:

Thesis Advisor _____

Dr. David Shonnard

Committee Member _____

Dr. Ezra Bar-Ziv

Committee Member _____

Dr. Michael Mullins

Department Chair _____

Dr. Tony Rogers

Date _____

Table of Contents

List of Figures

List of Tables

Acknowledgements

Abstract

The main objective of this research was to investigate pyrolysis and torrefaction of forest biomass species using a micropyrolysis instrument. It was found that 30-45% of the original sample mass remained as bio-char in the pyrolysis temperature range of 500 - 700˚C for aspen, balsam, and switchgrass. The non-char mass was converted to gaseous and vapor products, of which 10-55% was water and syngas, 2-12% to acetic acid, 2-12% to hydroxypropanone, 1-3% to furaldehyde, and 5-15% to various phenolic compounds. In addition, several general trends in the evolution of gaseous species were indentified when woody feedstocks were pyrolyzed. With increasing temperature it was observed that: (1) the volume of gas produced increased, (2) the volume of CO_2 decreased and the volumes of CO and CH_4 increased, and (3) the rates of gas evolution increased. In the range of torrefaction temperature (200 - 300˚C), two mechanistic models were developed to predict the rates of CO_2 and acetic acid product formation. The models fit the general trend of the experimental data well, but suggestions for future improvement were also noted. Finally, it was observed that using torrefaction as a pre-curser to pyrolysis improves the quality of bio-oil over traditional pyrolysis by reducing the acidity through removal of acetic acid, reducing the O/C ratio by removal of some oxygenated species, and removing a portion of the water.

1 Introduction

The production of biofuels from biomass has gained accelerated interest in recent years as these fuels are becoming increasingly economically-viable, renewable, and carbon-neutral energy sources. One reason for this renewed interest derives from new policy and legislation such as sustainable biofuel targets in the US Energy Policy Act (EPA 2005) and Energy Independence and Security Act (EISA 2007). In addition to these policies, renewable energy/fuel sources are substantially better for the environment and economy because they are renewable, reduce environmental burdens over petroleum fuels, and provide a broader range of marketable products.

Currently the largest biofuels production effort is in the production of corn ethanol. Currently, ethanol (produced almost entirely from corn) displaces over 4.6 billion equivalent gallons of gasoline and fueling almost 5.5 million flexible fuel vehicles (DOE 2011). Corn ethanol as a fuel a very important stride in biofuels production, but is capped at 15 billion gallons per year (BGY) as stated in the EISA. This Act also mandates 36 BGY of biofuels must be blended with traditional gasoline by 2022. Of these 36 BGY, 21 must be classified as "Advanced Biofuels", or biofuels that exhibit significant environmental benefits and are derived from non-corn starch feedstocks. In order to address these requirements, much effort has been place into: (1) producing ethanol from non-corn starch sources, and (2) producing a viable biofuels that are different than ethanol.

Today, corn ethanol is produced through biochemical conversion steps using acid, enzymes, and organisms to perform the required saccharification and fermentation steps. Ethanol can, however, be produced from any material that contains fermentable sugars, such as any lingocellulosic biomass. Because wood is an abundant, and largely a sustainably managed resource, it is an excellent candidate for such an alternative feedstock. An investigation of this process with poplar and willow as feedstocks is included as Appendix A.

In addition to ethanol, biomass-oil production is emerging as a mature research topic. These fuels can also contribute to the "Advanced Biofuels" mandate, and are becoming of great interest. Biomass-oils can be produced using a thermochemical conversion process called pyrolysis, and can be used to create true hydrocarbon fuels comparable to traditional gasoline and diesel.

1.1 Pyrolysis-Oil from Pyrolysis

Biomass oils (Pyrolysis-Oil) can be produced from biological materials through a process called pyrolysis. Pyrolysis is thermal degradation in the absence of oxygen. This is the key feature to pyrolysis - and what differentiates it from simply burning material. The process generally creates three products: a dense bio-oil, a low heating value gas stream, and a solid bio-char.

The bio-oil is usually a dark and viscous oil, not unlike heavy petrol-oil, and can have a strong smoky odors depending on the original feedstock (Czernik and Bridgwater 2004). This oil is usually very acidic (pH around 2.5) and contains mostly water (15-30 wt%) and polar organics (75-80wt%) (Bridgwater et al. 1999; Mohan et al. 2006). Some of these polar organic compounds, as demonstrated in this research and existing literature (Jackson et al. 2009; Patwardhan et al. 2009; Patwardhan et al. 2011), include: hydroxyaldehydes (such as glycolaldehyde), hydroxyketones, monomer sugars (such as glucose and xylose), sugar varients (such as levoglucosan), carboxylic acids (such as acetic and formic acid), and phenolics or cyclic compounds. This bio-oil can be directly used for heating and electricity generation (Fan et al. 2011), or undergo further refining to a true hydrocarbon transportation fuel.

The gas-phase product stream usually contains a mixture of low-value gases (CO, CO_2) with small amounts of higher energy-value combustibles (methane, ethane, hydrogen). Synthesis gas (syngas) has similar heating properties to natural gas, and could be used in similar applications. Syngas is usually combusted and used to fulfill heating needs, but can also be upgraded to other products such as ammonia or methanol (Zhu et al. 2011).

The solid residue remaining after pyrolysis (or torrefaction at low temperatures, 200-300˚C), is referred to as char, bio-char, or bio-coal. Bio-coal has similar properties to traditional coal, and in many cases can be used as a 'drop-in' replacement in existing power generation infrastructure.

1.2 Pyrolysis Technology Today

Slow pyrolysis is used in coke and charcoal production, while fast pyrolysis has been used for liquid bio-oil production since its discovery around 1980 (Mohan et al. 2006). Within the last decade, several companies, Ensyn Technologies and Envergent, have developed technologies to accomplish this with their Rapid Thermal Processing (RTP) methods. Although a known process for a long time, there is only limited scientific knowledge available in the fast pyrolysis area.

1.2.1 Review of Pyrolysis Literature

In reviewing pyrolysis literature, one of the most prominent review articles compiled was done by Mohan et al. (2006). After describing material such as the structure of biomass and the different pyrolysis methods, properties of bio-oil are summarized in this review. These properties were observed through Gas Chromatography / Mass Spectroscopy (GC-MS), and High Pressure Liquid Chromatography followed by Electrospray Mass Spectroscopy (HPLC/ES-MS) (Mohan et al. 2006). Crude bio-oil is described as a very dark liquid containing 15-50% water, having a density of approximately 1.2 kg/L, a pH around 2.5, and having a viscosity between 25 and 1000 cSt depending on the feedstock and moisture content(Mohan et al. 2006). It is also noted that the bio-oil cannot be completely re-vaporized once it has been condensed from its original vapor state, and has inconsistent aging properties (Mohan et al. 2006). Fast pyrolysis of wood is displayed as producing 75% liquid product, 12% char product, and 13% gaseous product and biomass gasification (higher temperatures for longer times) has yields of 5%, 10%, and 85%, respectively (Mohan et al. 2006).

Several factors that impact the products from pyrolysis were also discussed by Mohan in his review. Higher heating rates were found to decrease char yield, increase the bound oxygen within the chars, and decrease the carbon content of chars (Mohan et al. 2006). This is a very important conclusion, as it implied that using a higher heating rate during pyrolysis will create pyrolysis oil with a lower O/C ratio, easing the burdens of upgrading pyrolysis oil. It was also noted that the presence of alkaline cations (K^+, Li^+, and Ca^{2+}) affects pyrolysis decomposition mechanisms (Mohan et al. 2006). It was stated that these ions cause monomer unit fragmentations, where usual depolymerization would occur in natural biomass chains (Mohan et al. 2006). The influence of these ions also caused species to produce less bio-oil, less anhydrosugars, more acetic acid, and more char (Mohan et al. 2006). Light acid washing to perform ion exchange within the feedstocks was noted to remedy these adverse impacts.

The remaining knowledge in the area of biomass pyrolysis has mostly been obtained through GC/MS and Fourier Transform Infrared Spectroscopy (FTIR) analysis methods. In addition, the existing literature mostly examines either pure biomass components (cellulose, hemicelluloses, and lignin) or specific waste products such animal bedding, rice husks, etc. Very few studies have looked at a detailed speciation / quantification fast pyrolysis analysis of the pure lignocellulosic biomass feedstocks studied here. Because of the specific and applied nature of this research area, the literature review in this thesis will be focused on the pyrolysis of the pure components of typical lignocellulosic (woody) biomass (cellulose, hemicelluloses and lignin) as they are the closest relevant content.

Although pyrolysis of pure wood components is different than the pyrolysis of complex mixtures and structures, it is important to note the major compounds formed from cellulose, hemicelluloses, and lignin. Fast pyrolysis of corn stover and pure biomass components has been studied in detail by Dr. Robert Brown and his research group from Iowa State University. In the fast pyrolysis of pure cellulose, they found some of the major compounds found in the products include: formic acid, glycolaldehyde, 2-furaldehyde, 2-furan methanol, 3-furan methanol, levoglucosan – pyranose, char, and gases (Patwardhan et al. 2009). Although the mass fraction of these compounds differed

slightly between the different sources of cellulose studied, these compound classes remained present in all samples. In a study of hemicellulose pyrolysis, the same group found that the major detectable compounds partly include acetaldehyde, formic acid, acetic acid, acetol, 2-furaldehyde, xylose, other anhydro-sugar variants, char, and gases (Patwardhan et al. 2011). For the pyrolysis of lignin, a collaboration between the National Center for Agricultural Utilization Research and the Eastern Regional Research Center found that the various products include toluene, ethylbenzene, 2-methylphenol, 3-methylphenol, ethylphenol, 1,2-benzendiol, dihydrobenzofuran, char, and gases (Jackson et al. 2009). Clearly, these products of fast pyrolysis are indicative of the source or material from which they were derived, either carbohydrate or lignin.

These studies can be summarized in a few key findings: (1) cellulose and hemicelluloses produce light molecular weight organic acids, aldehydes and other oxygenated species, and anhydrosugars, and (2) lignin yields mostly heavier cyclic aromatic (phenolic) compounds.

1.2.2 Commercial Production by Pyrolysis

Production of bio-oil with pyrolysis is becoming a reality as facilities like the one owned by Ensysn Technologies are being planned and built. To date, the facility owned and operated by Ensyn Technologies is the world's largest production-scale fast-pyrolysis facility (REF 2010). The facility is located in Renfrew Ontario, and has a nominal operating capacity of 150 tonnes per day of wet biomass, but has demonstrated larger capacities (Ensyn 2011). This facility uses hot sand as contact media to convert the biomass into gaseous, vapor and solid char products at a conversion rate of about 75% for the vapor-derived bio-oil (Ensyn 2011). Although much about this process is classified and confidential, it clearly demonstrates the potential commercial viability of the technology to create merchantable products.

1.3 Torrefaction Processing

Torrefied biomass is currently of significant interest for applications in energy systems, in particular for power generation in coal-fired plants and as a feedstock for biomass-based technologies. In 2011, there were at least 4 published reviews of torrefaction, its current technology, and its applications to energy applications(Chew and Doshi 2011); (Boardman et al. 2011); (Ciolkosz and Wallace 2011); (van der Stelt et al. 2011). Torrefaction is similar to pyrolysis in that it is a thermal treatment in the absence of oxygen. Torrefaction, however, takes place at lower temperature than pyrolysis, usually in the range on 200-300˚C.

Torrefaction of wood and other biomass feedstock has been shown to improve their properties for energy applications. Wood torrefied at 300°C for 10 min decreases the oxygen content from 45.1% to 36.3%, increases the carbon content from 47.2% to 55.8%, and increases the lower heating value (LHV) from 17.6 MJ/kg to 21.0 MJ/kg (van der Stelt et al. 2011). The torrefied products of lignocellulosic biomass has been described as 70-90% solids, 6-35% liquid, and 1-10% gas on mass basis (Ciolkosz and Wallace 2011). The solid portion of the product is made of ash, char, original and modified sugar structures, and some newly formed polymeric structures (Boardman et al. 2011). The liquid product is comprised of water, organic compounds (acids, alcohols, furans, ketones), and terpenes, phenols, and fatty acids (Boardman et al. 2011). The remaining gaseous product portion is made of H_2, CO, CO_2, and CH_4 (Boardman et al. 2011). It was also noted that although the energetic properties of feedstock appear to improve, economic investigation should also be considered due to torrefaction processing costs themselves and the need to pelletize or briquette the torrefied biomass (Ciolkosz and Wallace 2011)

There has been a lot of work done with torrefaction chemistry, but due to its complexity there are many different competing ideas and a clear chemical pathway still needs to be identified (Chew and Doshi 2011). It is generally upon agreed, however, that during torrefaction the product evolution and mechanistic changes are due mainly to the hemicellulose fraction of the wood (Boardman et al. 2011); (Chew and Doshi 2011);

Yang et al. 2007). Within wood hemicelluloses, polymerized xylan is the primary component (Ciolkosz and Wallace 2011). To date, efforts to model torrefaction decomposition have been centered around models including one step global models, three parallel reactions models, two step consecutive models, and two parameter reactions models (Chew and Doshi 2011).

1.4 Research Objectives

The introduction and literature review above have led to the overall research objectives addressed in this work. Existing work in both thermal treatment processes, pyrolysis and torrefaction, are continuously evolving. Research objectives were created to supplement the existing literature to include processing of hardwoods (aspen, willow, poplar, and red maple), softwoods (balsam), and herbaceous energy crops (switchgrass). More specifically, fast pyrolysis and torrefaction processing objectives in this research include:

1. processing of multiple forest feedstocks by fast pyrolysis and torrefaction
2. measuring the distribution of solid char and gaseous/vapor phases in the torrefaction and pyrolysis products
3. identify and quantify gaseous and vapor products
4. improvement of pyrolysis-oil properties through the use of torrefaction as a pretreatment method
5. modeling kinetics for production of gaseous and vapor species from fast pyrolysis and torrefaction.

2   Pyrolysis of Woody Biomass

2.1 Introduction

It has been observed that there are well over 300 organic compounds present in pyrolysis oil (Mohan et al. 2006). This presents a rather daunting task to quantify and indentify these compounds. Because of this, it seems that the only solution is to use an analytical method/instrument, and focus on the most abundant species. The use of GC/MS analysis to analyze the products of pyrolysis has had promising results, in terms of speciation and quantification, and has become a prominent method in indentifying and quantifying the major products (Jackson et al. 2009; Patwardhan et al. 2009; 2010; Dizhbite et al. 2011; Patwardhan et al. 2011).

2.1.1 Research Objectives

In order to supplement existing literature, this work was performed using pure wood species. To gain at least a preliminary understanding of the processability of woody feedstock with pyrolysis, several key results need to be investigated including the product phase distribution, bio-oil species identification, and products formed during biomass gasification.

2.2 Materials and Methods

2.2.1 Experimental Equipment

The micro-pyrolysis reactor used in this work was a model 5200HP Pyroprobe created by CDS Analytical. The gas chromatograph was a Trace GC Ultra (Model K8880181) by Thermo-Finnigan (now ThemoFisher) and was operated with a 30 meter RXI-5MS fused silica (low polarity phase, Crossbond® 5% diphenyl/95% dimethyl polysiloxane) capillary column by Restek. The mass spectrometer was also by ThermoFinnigan (now ThermoFisher) and is a model Trace DSQ. The microbalance used during the experiments was a model CM5 created by Citizen Scales Inc. and has a readability of

1µg. Equipment used in biomass preparation includes a W.S. Tyler rotap (model RX-29, serial 9774), dying oven, and a small scale Thomas Wiley® knife mill(NR. 3557524 359264).

2.2.2 Biomass Preparation

Debarked biomass samples used in this experiment were obtained from Dr. Christopher Webster in the School of Forest Resources and Environmental Science (SFRES) at MTU (aspen, balsam, red maple), from Dr. Raymond Miller of the Michigan State University Forest Biomass Innovation Center in Escanaba, MI (poplar, willow) and from Dr. James McMillan of the National Renewable Energy Laboratory (NREL) (switchgrass). Prior to use within the experiments, each biomass sample was dried and milled into small pieces. Drying was performed through heating in a drying oven at 105˚C until a difference in mass was no longer detected. The drying was performed in accordance with NREL's LAPS (NREL 2008). A small scale hammer mill, located at MTU in SFRES, was used to grind the dried biomass to an appropriate range of sizes. A rotap equipped with a range of sieve trays was used in the particle size differentiation. The sizing was performed in accordance with NREL's LAPs (NREL 2008) with modifications to adjust for appropriate sieve sizes (sizes larger than 32 Tyler Mesh, but smaller than 28 Tyler Mesh or approximately 500 - 599 microns).

2.2.3 Moisture Content Analysis

The moisture contents of the feedstocks were determined with a drying oven. In this procedure, the oven was held at a constant temperature of 105˚C and the sample masses were recorded over time.   When the mass stopped decreasing, the material was determined to be completely dry. The moisture content was calculated as the difference between the samples initial weight minus its final weight, assuming that the entire sample mass loss was water. These results are important, because when the samples are prepared for pyrolysis they contain moisture, whereas when they are weighed after the pyrolysis cycle they are completely dry. This allows the mass balance to account for the bound

moisture leaving the feedstock, that isn't from dehydration reactions. The moisture content of the feedstocks range from 5.0-8.5% in these pyrolysis experiments.

2.2.4 Direct Pyrolysis-GC/MS Experiment

Experimental trials began when an empty quartz vial (a capillary used to hold the wood biomass sample for fast pyrolysis) was loaded into the sample pyrolysis probe along with two quartz wool plugs inserted into each end of the vial. Quartz wool acts as a filter on either end of the vial, which is a hollow cylinder, allowing He gas to flow through it while retaining the biomass and solid residues. After the empty vial was loaded into the micropyrolysis reactor with the probe, the materials underwent a pyrolysis cycle identical to that which was run on the biomass samples. This procedure, referred to as a *blank*, was performed before each experimental trial as a quality control method. With a process identical to that which was run on the biomass, it was demonstrated that the materials are perfectly clean and there was no residual matter anywhere in the system. Once it was established from the resulting chromatogram that the only MS signal was representative of noise, and low bleed from the fused silica column in the GC, the feedstock trial could begin.

Once a successful blank was obtained, biomass particles were loaded into the clean quartz reactor vial between the two quartz wool plugs (approximately 0.5-1.0 mg sample size). The vial containing the biomass sample was then inserted into the pyrolysis reactor via the sample probe. Once inside, the vial was immediately purged with 25 mL/min inert helium gas. The targeted pyrolysis temperature was automatically obtained at very high heating rates by calculating the resistance of the filament at the set-point temperature, and supplying the correct voltage. When the sample was pyrolyzed it was very rapidly (>999˚C/second) heated up to an experimental temperature (500, 600, or 700˚C) and held there for 15 seconds. There was an interface time (2 minutes) after the heating begins where the inert gas passes through the sample probe, quenched the products, and carried any resulting gases and vapors through a heated transfer line to the gas chromatograph and then to the mass spectrometer for analysis. When the sample began to heat, the MS began to analyze and record data.

The GC oven temperature was initially set to a low temperature (30°C) to allow the vapors to condense and adsorb to the fused silica surface within the column. Some species, namely the gases and a few light organic acids, do not get retained by the column and are carried straight to the MS for analysis. For the remaining species, however, the oven was then slowly heated to remove the compounds at their respective retention times, which are conveyed to the mass spectrometer with the helium carrier gas. Here, the molecules were fragmented using electrons generated with a heated filament. The resulting fragments were recorded as a mass spectrum. Mass spectra were then related to spectra of known compounds in the National Institute of Standards and Technology (NIST) libraries contained in the GC/MS software or the NIST Chemistry WebBook (NIST 2011), and the compounds were identified. The probability of a match was also reported. This probability determines the accuracy of the library search. Furthermore, the GM/MS software integrates the area under each identified peak, which was used to estimate the relative mass of each compound identified. Figure 2.1 shows a simplified flow diagram for the Pyrolysis - Gas Chromatography - Mass Spectroscopy (PY-GC-MS) experiment apparatus used. The three analytical instruments are interfaced with heated transfer lines, and high purity (99.999%) helium is used to carry evolving vapors through the system.

Figure 2.1: Simplified flow diagram for fast pyrolysis and torrefacction experiments.

2.2.5 Gravimetric Quantification

Throughout these experiments, measurements were taken to obtain a gravimetric mass balance. For this procedure, some of the biomass sample was placed into a weighing tin and a mass was recorded using the analytical microbalance. One of the wool plugs from a clean blank was then removed so the previously weighed wood sample could be loaded into the vial. The discrete particles were carefully placed into the vial. The wool plug was placed back into the vial after the sample was loaded. The mass of the weighing tin and feedstock sample was then taken again, to get the mass of wood added to the vial by difference. The mass of sample added to the vial was then converted to a dry basis with the moisture content of the feedstock. At this point the sample vial could be placed into the probe and the PY-GC/MS portion of the experiment could continue. The vial was then weighed again after the experiment to obtain the mass of the sample that was

12

pyrolyzed (representative of the pyrolysis oil and gases) by mass difference. The difference between the dry biomass added to the sample vial and mass of sample leaving during pyrolysis was equal to the pyrolysis char.

2.3 Results and Discussion

2.3.1 Phase Distribution

Figure 2.2 shows the combined distribution of pyrolysis oil and gas for different feedstocks over a large range of experimental temperatures. The feedstocks shown were chosen to represent hardwoods (aspen), softwoods (balsam), and herbaceous energy crops (switchgrass). The remaining weight percent represents the mass remaining in the experimental vial as bio-coal (char). Also included in the figure is a trend for wood pyrolysis between 400 and 600°C from the literature (Bridgwater et al. 1999). The figure shows that there are large amounts (50-70%) of bio-oil and gas products that can be produced from the investigated feedstocks at the targeted experimental conditions. While our data suggests that the yields are lower than previous
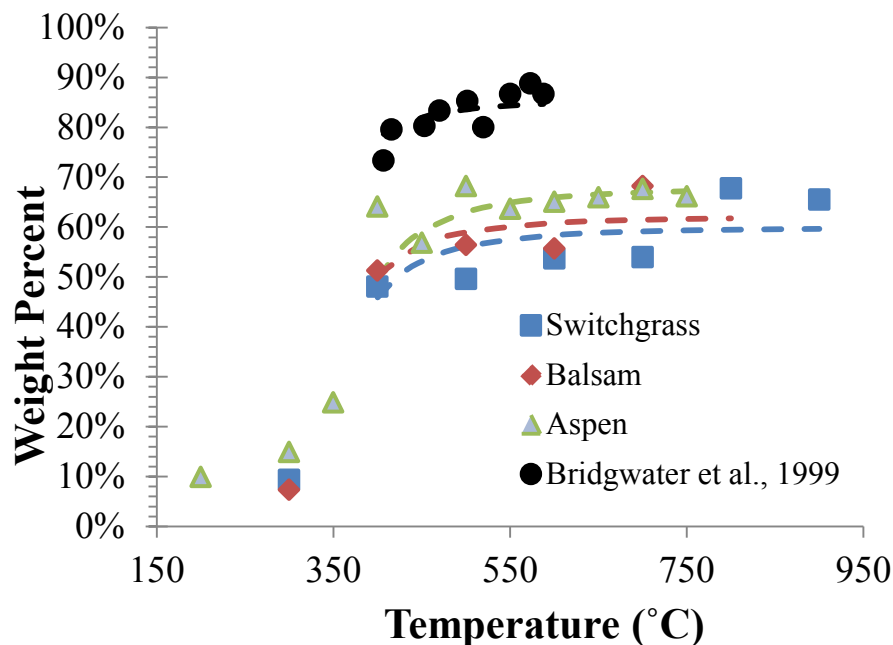
Figure 2.2: Average weight percents of combined bio-oil and gas products for aspen, balsam, and switchgrass.

13

studies have found, the same general trend is observed in the temperature regions of interest for bio-oil production (500-700˚C). This effect could be explained by the influences of alkaline cations due to biomass sample being processed "as-received".

To get a more complete understanding of the phase distribution over a wide temperature range, aspen was processed over additional temperature increments. A sigmoid-curve model (S-curve) (Ledvij, 2011) was fit to data to obtain a complete picture of phase distribution as a function of temperature. This type of model was chosen because the mass loss observed by the sample has clear physical boundaries, starting with loss of feedstock moisture, and ending with loss of all volatile compounds. Between these physical constraints, dynamic behavior was expected and observed. Figure 2.3 shows the data for aspen with an S-curve fit. The equation for this fit is shown below.

$$wt\% = 66.4\% + \frac{(66.4\% - 9.9\%)}{1 + exp\left[-\frac{(T - 386.7˚C)}{35.6˚C}\right]} \tag{1}$$

In addition, Figure 2.3 illustrates how the char formation (thus oil and gas) is affected by pyrolysis temperature through the degradation stages of cellulose, hemicelluloses, and lignin. At temperatures at or below 200˚C there is very little reactivity in the biomass, and the change in mass can be attributed to loss of initial feedstock moisture. This moisture would appear in the collectable bio-oil. Over the hemicellulose decomposition range, the mass appears to decease another 5-10% which can be attributed to the non-char portion of hemicellulose. Within this range, thermogravimetric analysis (TGA) studies have shown that approximately 80 weight percent of hemicelluloses (xylan) is lost (Boardman et al. 2011). Similarly, the area within and just following the cellulose decomposition range can be seen to have an impact of approximately 30-45% which attributed to the non-char portion of cellulose. TGA has shown around 90 weight percent loss in cellulose within this range (Boardman et al. 2011). The remaining mass loss of 10-20% is justified by the conversion of lignin, which begins to degrade more fully after cellulose decomposition. Lignin has shown up to 60 weight percent loss up to 500°C
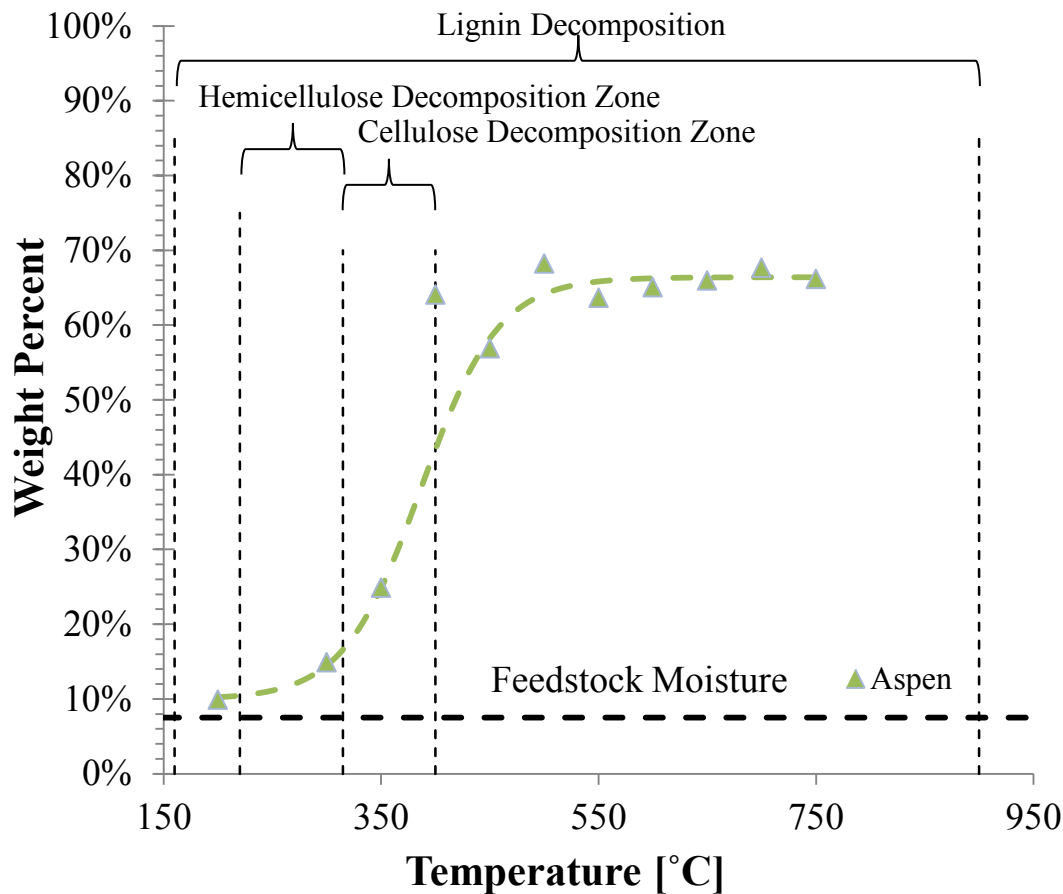
Figure 2.3: Average weight percents of combined bio-oil and gas products for aspen. Decomposition zones from (Yang et al. 2007).

through TGA (Boardman et al. 2011). These mass loss values compare favorably to the carbohydrate and lignin composition values of the wood. Yat et al. found the xylan (interpreted to represent hemicelluloses) content of the aspen sample to be 14.6%, the glucan (interpreted to represent cellulose) content to be 52.4%, and the lignin content to be 26.7% (Yat et al. 2008).

2.3.2 Gasification

Biomass gasification takes place more prominently with increasing pyrolysis temperature. Gasification is generally considered to take place at a temperature of 700˚C or greater. As the pyrolysis temperatures approach gasification ranges, the products were

observed to shift more towards light oxygenated compounds and gaseous species. This trend is explicitly demonstrated in Figure 2.4.

Figure 2.4 demonstrates that different temperatures of processing (represented as different colors) have many of the same compounds existing between pyrolysis processing at 500˚C, up to light gasification processing at 700˚C. Heavier molecules are generally seen at higher retention times. It can be seen that as processing temperature increases, the products at high retention times decrease, and product with low retention times increase. This implies that many of the heavier molecules such as phenolics or poly-phenolics (that would normally reside in the bio-oil) are further broken down into gaseous species as the processing temperatures rise. For clarity, some peaks at either end of the spectrum have had their apex marked with dotted lines. These same general trends in species shifting have been demonstrated in existing literature (Bridgwater et al. 1999; Mohan et al. 2006).
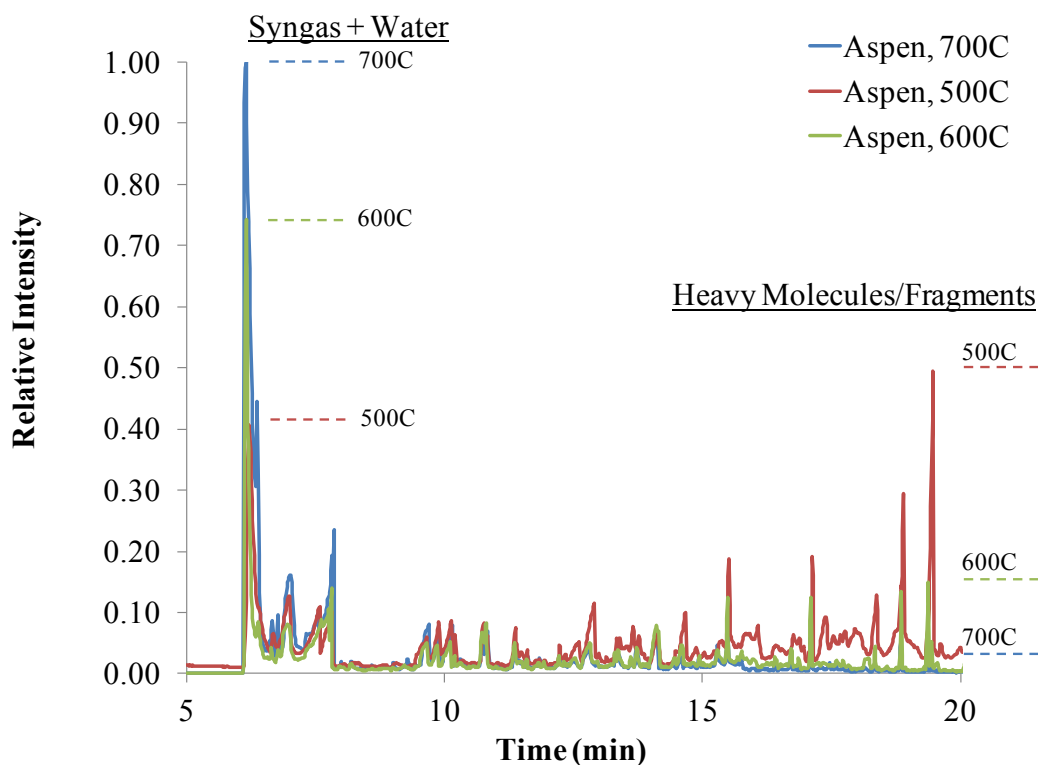
Figure 2.4: Change in product distribution for varying fast pyrolysis temperatures.

16

The following figures (2.5-2.11) show the gaseous breakdown for the investigated species as temperature increases from pyrolysis processing at 500˚C, up to light gasification processing at 700˚C. In addition to the aforementioned trends, these figures also illustrate that the species most generally affected by the temperature, are the formation of carbon monoxide and methane. Gasification of aspen to a very high temperature (900C) is shown in Figure 2.6 to more clearly demonstrate gasification trends. Hydrogen was also observed, but at very low quantities (<1.5% detectable area) even at the highest pyrolysis temperature. Due to this fact, analysis of hydrogen formation was excluded from this study. Figures 2.5-2.11 contain normalized data generated by MS over time. Normalization was performed by identifying the highest MS signal value among CO, CO_2, CH_4, and H_2 for all temperatures within a species, and dividing each data point by that magnitude (representative of the largest peak's height). Normalization for the total gas production was performed in an identical manner, but separately from the species figures. The normalized curve areas were then calculated with a traditional Riemann sum.

Figure 2.5 shows the evolution of gas species for aspen as processing temperatures increase. The total gas signal (top left) starts from a relative peak area of 0.047 at 500˚C and rises to approximately 0.051 at 600˚C, and to 0.081 at 700˚C. This increase in peak area is an indication that more gaseous species are evolving with increasing temperature. In addition, the shape of the overall gaseous peaks imply that at 500˚C the gaseous specious evolve at a slower rate (broader peak shape) than when the species are processed at 600˚C or 700˚C (much narrower peak). The additional images in Figure 2.5 show the gas-species breakdown at the various temperatures. CO_2 is the dominant gaseous species formed at 500˚C and 600˚C, but is slightly overtaken by CO at 700˚C.

Although the production of CO_2 in aspen (Figure 2.5) appears to be increasing with increasing temperature, the CO_2 integrated peak areas actually decrease with increasing temperature (0.077, 0.070, and 0.064, respectively). The CO_2 peaks are, however, increasing in peak height and narrowing with increased pyrolysis temperature. With the trends of peak area and shape for CO_2 it can be concluded that for aspen, increasing the pyrolysis temperature will: (1) evolve CO_2 at a faster rate, and (2) will decreasing the

17

production volume of CO_2. This implies that either the formation of CO_2 less favorable at higher temperatures, or the gas is being further degraded as it evolves.
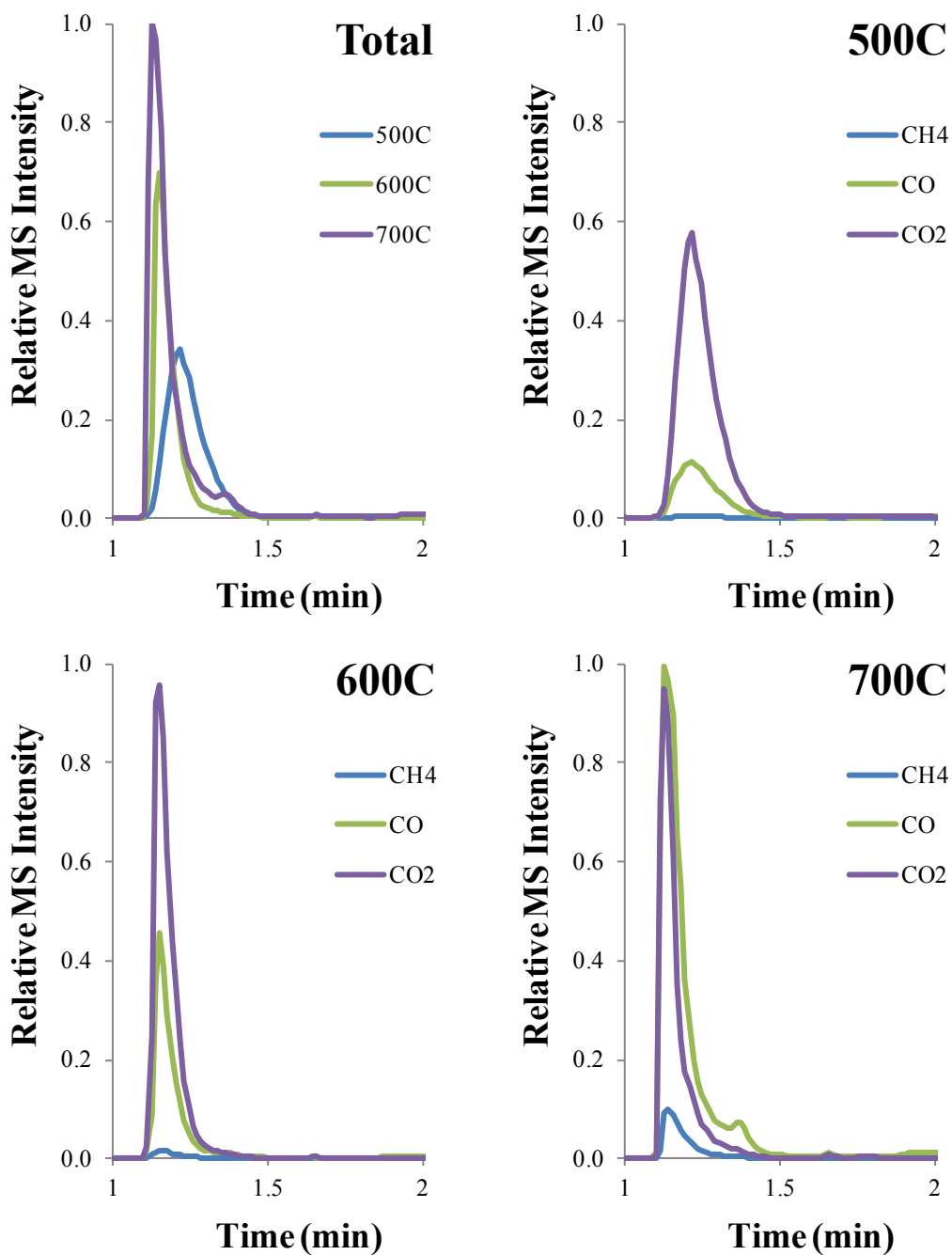
Figure 2.5: Effect of temperature on gaseous species yield for aspen.

The production of carbon monoxide in aspen (Figure 2.5) appears to have the largest change with increasing pyrolysis temperature of aspen. The relative peak areas are 0.018, 0.032, and 0.092 respectively. The dynamics of the CO peak also follow that of CO_2 – increasing in height and narrowing with increasing temperature. From these observations it is noted that for aspen, CO production is: (1) increasing with increasing temperature, (2) the rate of production is increasing with increasing temperature. These observations indicate that CO is favorable for production at higher temperatures. The increase of CO production with increasing temperature, and decrease in CO_2 production with increasing temperature could indicate that CO_2 is degrading into CO and O at these high temperatures.

There is very little CH_4 at 500˚C and 600˚C treatment of aspen (Figure 2.5), so it is hard to indentify a trend in production rate, but there are increases in produced volume with increasing pyrolysis temperature (0.001, 0.002, and 0.009 respectively). This concludes that CH_4 is also a favored gaseous product when increasing pyrolysis temperature of aspen, but not nearly to the extent of CO.

Figure 2.6 shows a sample of aspen that has been gasified at 900˚C. Similar to Figure 2.5, the plot shows MS signal normalized by maximum peak height over time. The peak areas for CO_2, CO, and CH_4 respectively are 0.060, 0.132, and 0.009. These peak areas continue the trends for increasing temperature mentioned above: (1) CO_2 decreases, (2) CO increases, and (3) CH_4 increases. In addition, small amount of hydrogen (peak area 0.003) is produced. Hydrogen was not observed with the lower pyrolysis temperatures discussed above, and seems to be a favored gaseous product as processing temperatures reach well into the biomass gasification range (700-1000˚C).

19
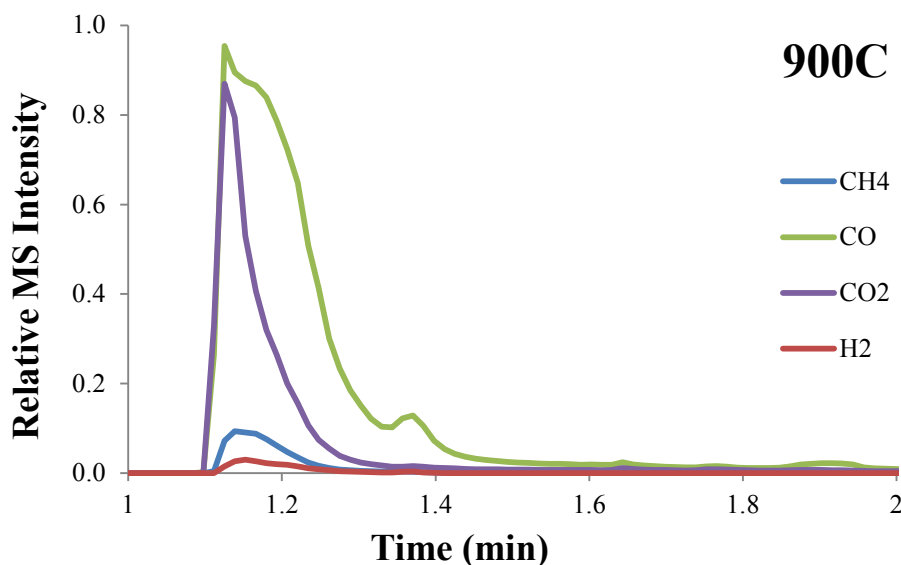
Figure 2.6: Aspen gasification at 900C.

Figure 2.7 shows the evolution of gas species for poplar as processing temperatures increase. These results are different from those of aspen because there is no production volume increase between 600˚C and 700˚C (.040 and 0.039 respectively). Similar to aspen, though, there is a clear gaseous evolution difference between 500°C and 600°C or 700°C due to the very broad 500°C peak. The major gas product at all temperatures is CO_2. In a similar analysis to above, CO_2 was observed to increase in production volume between 500°C and 600°C, but decrease between 600°C and 700°C (0.029, 0.042, and 0.039 respectively). Examination of the peak shapes conclude that CO_2 is produced faster with increasing temperature. CO and CH_4 production follow the same trends with increasing temperature as discussed for aspen: (1) volume increases (0.008, 0.010, and 0.012 for CO, 0.0006, 0.0010, and 0.0013 for CH_4), (2) rate of production increases. Although the reason for the CO_2 deviation is unknown, it is again clear that CO and CH_4 are favorable products for gasification of this feedstock.

Figure 2.7: **Effect of temperature on gaseous species yield for poplar.**

Figure 2.8 shows the evolution of gas species for balsam as pyrolysis temperatures increase. The overall gas production results are different from those of aspen and poplar. Here, there is only a small increase in total gas production with increasing processing temperature (0.067, 0.069, and 0.082 respectively). In addition, total gas production for balsam stands out from the previous feedstocks because the gaseous species appear to evolve at roughly the same rate despite the temperature (peak widths are about the same regardless of temperature). This is an interesting result, and might be influenced by the difference in structure between hardwood and softwoods. For balsam, the species production volumes follow the trends established from aspen. CO_2 production decreases (0.072, 0.059, 0.057), CO production increases (0.055, 0.069, 0.095), CH_4 production increases (0.002, 0.004, 0.007). As with the total gaseous production, the kinetics of the individual species don't appear to be affected by temperature because the shape of the evolution curves remain fairly consistent. The most abundant product here is CO_2 at 500°C, but changes to CO for 600°C and 700°C.

Figure 2.9 shows the gaseous evolution for red maple. The total gas production trends that can be identified here resemble those from balsam; there is a slight volume increase with temperature (0.082, 0.086, and 0.100) but the overall rate of gas evolution isn't influenced by temperature. Again, the species volumetric production tends to follow those identified from aspen: CO_2 production decreases (0.088, 0.078, 0.077), CO production increases (0.078, 0.093, 0.122), CH_4 production increases (0.007, 0.010, 0.011). Although the overall gas production rates seem to be identical between processing temperatures, this seem to be the case because the rate of CO_2 production is increasing slightly (peak narrowing) and the rate of CO production is decreasing (peak broadening). The rate of CH_4 production appears to increase slightly with pyrolysis temperature. The most produced gas here is the same as balsam, CO_2 at 500°C, but CO is the major product at 600°C and 700°C.

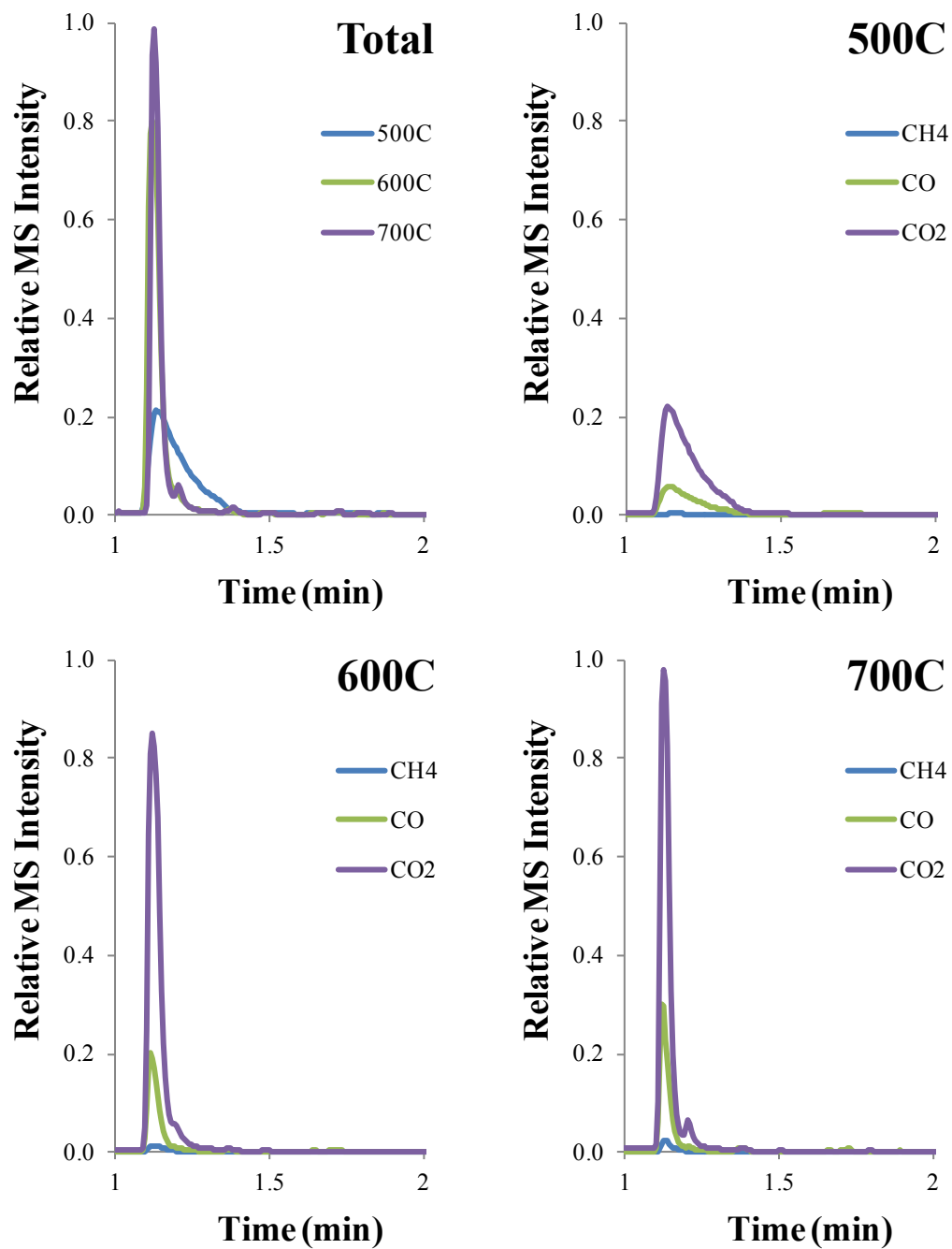**Figure 2.8: Effect of temperature on gaseous species yield for balsam.**
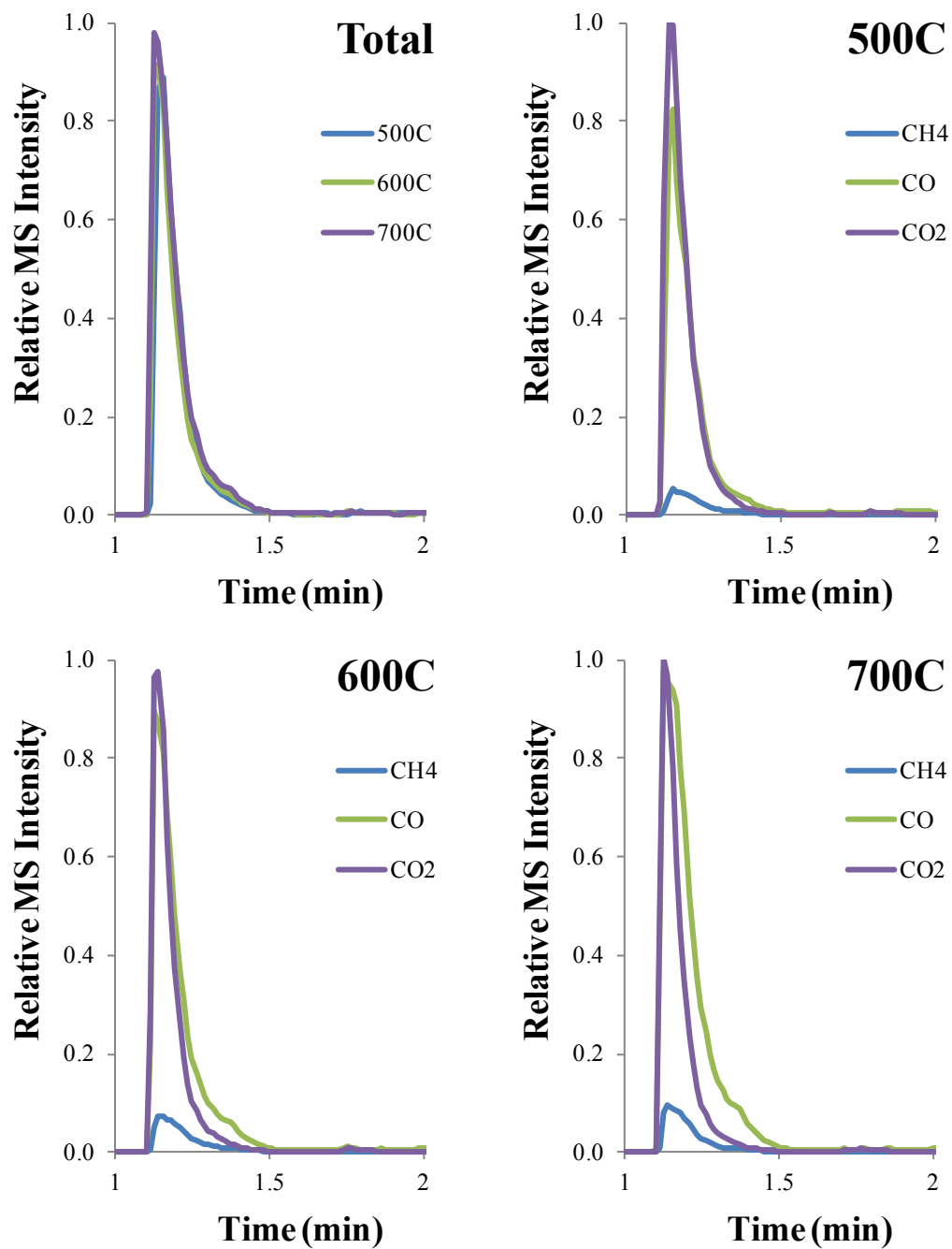
Figure 2.9: Effect of temperature on gaseous species yield for red maple.

Figure 2.10 shows the evolution of gas species for willow as processing temperatures increase. The rate of overall gas production increases with temperature similar to aspen, but the total volume production does not have an identifiable trend (0.038, 0.042, and 0.031). The species production rates are also similar to aspen (increasing with temperature), but, as with the total volume production, trends are hard to identify for species production (CO_2: 0.045, 0.049, 0.031, CO: 0.014, 0.017, 0.017, CH_4: 0.0010, 0.0014, 0.0011). The most abundant gas species for willow is CO_2 in all cases.

Finally, Figure 2.11 shows the gaseous evolution for switchgrass. The total gas production rate trends are similar to red maple and balsam, and don't appear to be influenced by temperature. The total gas production increases with temperature (0.036, 0.096, 0.108). In addition, all three gas species increase in volume with temperature (CO_2: 0.037, 0.094, and0.095, CO:0.030, 0.080, and 0.101, and CH_4: 0.002, 0.007, and 0.009). The evolution rates of CO and CO_2 appear to be increasing with temperature, but it is hard to identify a trend for CH_4. Here the major evolution species is CO_2 at 500°C and 600°C, but CO is the most abundant gas formed at 700°C.

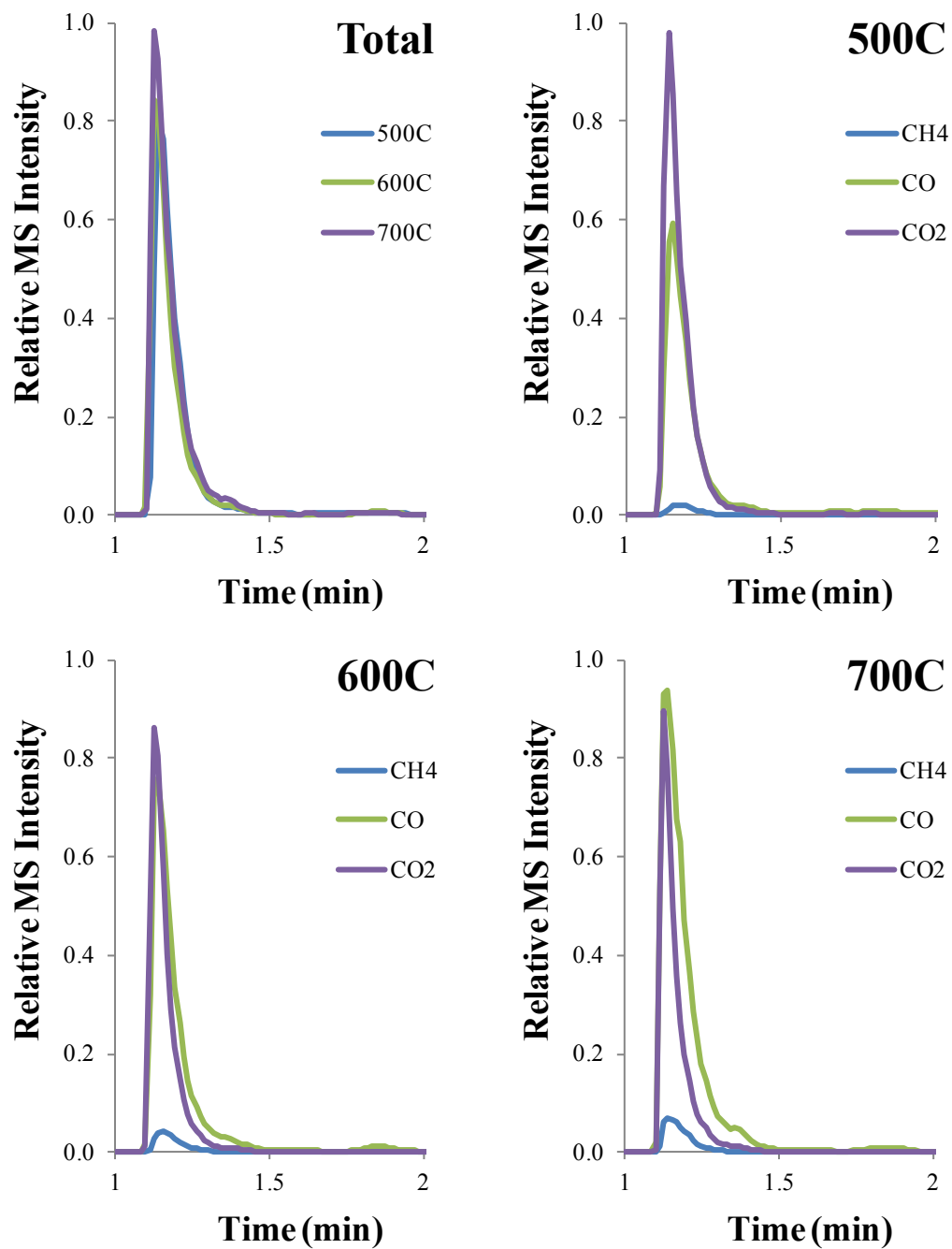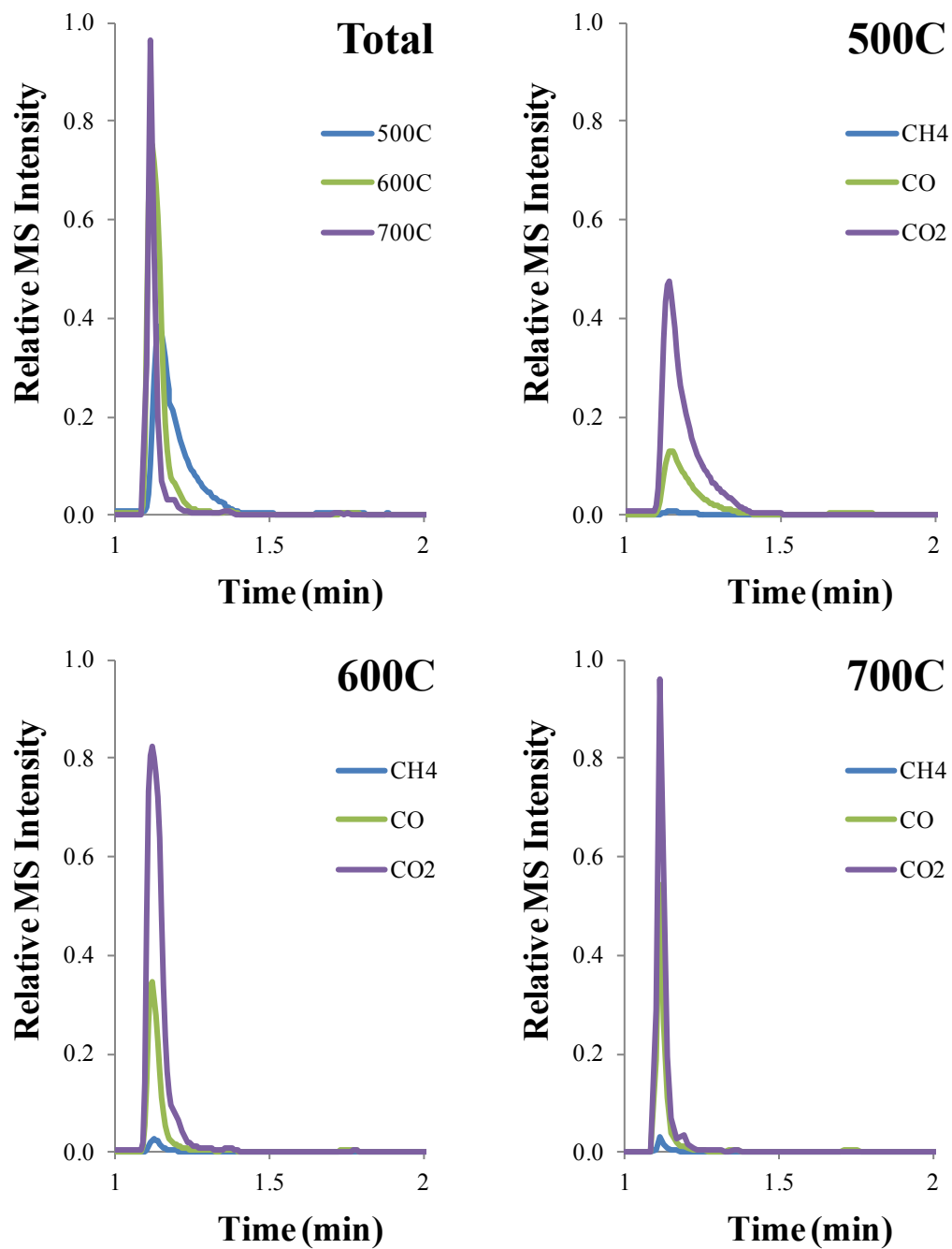**Figure 2.10: Effect of temperature on gaseous species yield for willow.**
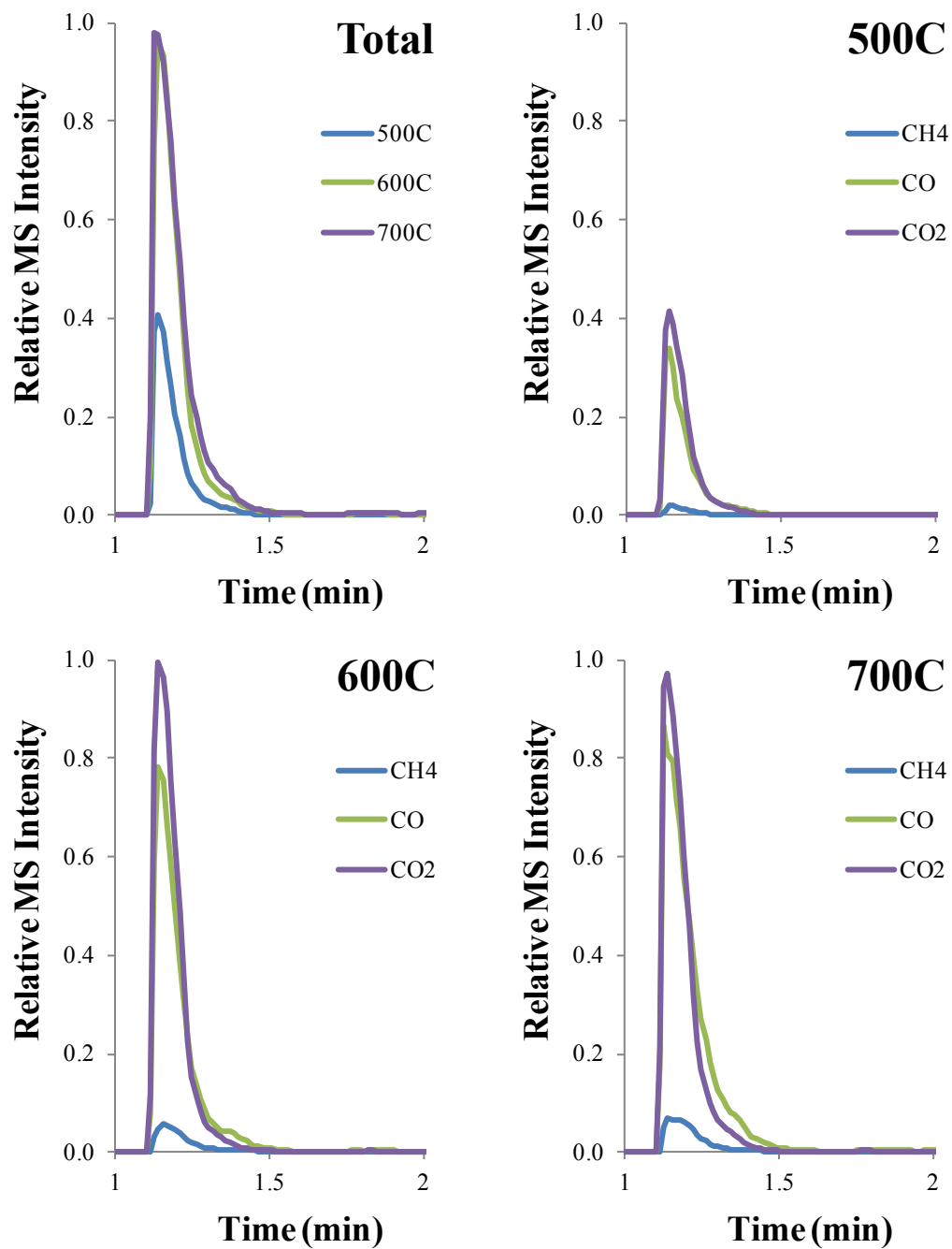
Figure 2.11: Effect of temperature on gaseous species yield for switchgrass.

2.3.3 Product Identification and Quantification

With over 300 compounds (Mohan et al. 2006) expected to reside in the bio-oil, it is a daunting task to characterize and quantify the product distribution. From the work reported, however, it is noticed that the majority (approximately 75%) of mass appears in only a small number of components. Based on the relative peak areas as detected by the GC/MS, it was found that the major constituents in the oil phase are glycolaldehyde, acetic acid, acetol, aldehydes (such as 3-furaldehyde), and other well-known heavy products (such as 3-hydroxycarbofuran and phenolics). Many of the fast pyrolysis trials yielded very similar compounds at similar retention times. Because of this, a chromatogram of aspen will be displayed here as a common representative, while full experimental trial data from this section are included as Appendix B.

Figure 2.12 shows a chromatogram from a trial of aspen at 600°C. Light oxygenated materials typically have lower retention times and elute more quickly than heavy molecules with more complex structures. The first materials to be detected are the gaseous species and water (contained within peak 1). The second identified peak is hydroxyl acetaldehyde and is likely formed from the degradation of hemicelluloses (Patwardhan et al. 2011). This is identifiable from the acetyl group that is typically attached to the backbone structure of hemicelluloses. Similarly, peak 3 (acetic acid) likely comes from the breakdown of hemicelluloses. Peaks 4 and 5 represent 2-propanone, 1-hydroxy and 3-furaldehyde respectively and come from either cellulose or hemicelluloses decomposition (Patwardhan et al. 2009). Peak 6 is 3-hydroxycarbofuran, and likely is formed from the decomposition of lignin due to its cyclic structure (Jackson et al. 2009). Many of the compounds with large retention times have complex structures, making them difficult to identify. Although many library matches could not be identified with high certainty, many of these compounds were recognized to be cyclic (or phenolic) compounds from their mass spectra fragmentation patters. These compounds are produced from feedstock lignin.

Aspen, 600˚C

1. CO, CO_2, H_2O
2. Acetaldehyde, hydroxy-
3. Acetic acid
4. 2-Propanone, 1-hydroxy-
5. 3-Furaldehyde
6. 3-Hydroxycarbofuran
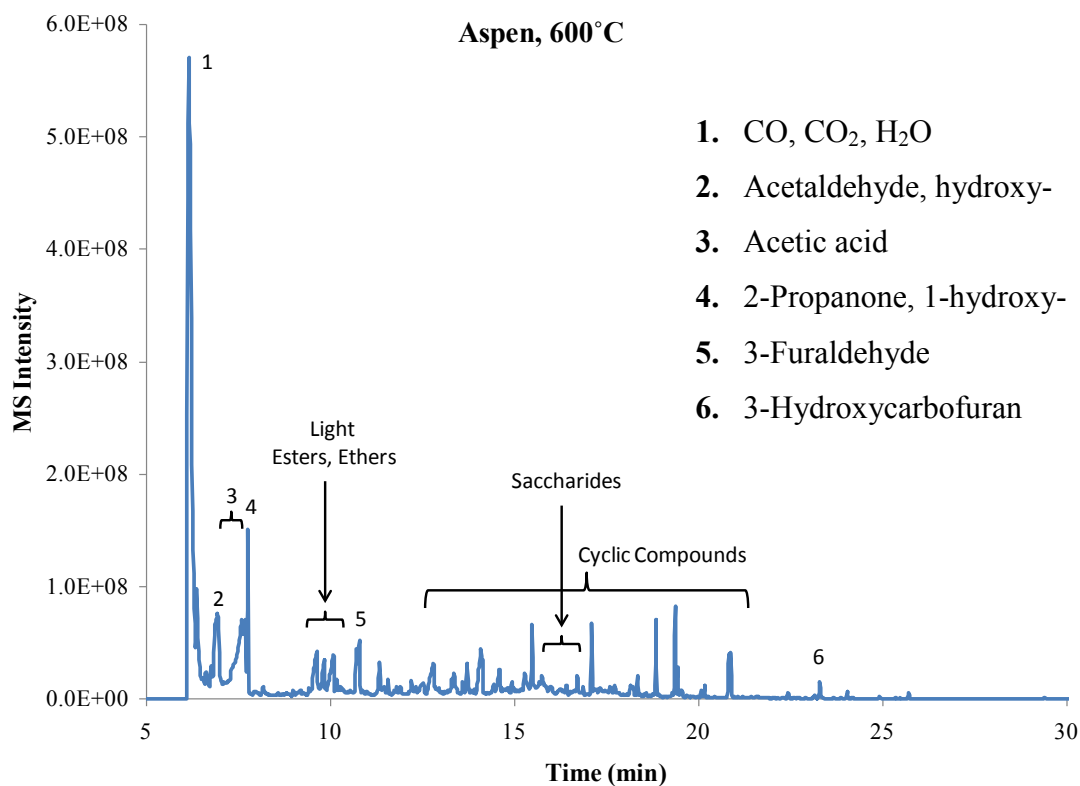
Figure 2.12: Chromatogram for an aspen trail at 600˚C.

Tables (2.1 - 2.6) form a summary for peak identification for pyrolysis of all feedstocks at different temperatures. The compounds are listed in ascending order according to their retention times (RT), and are presented with their relative peak areas. The relative peak area values are obtained by dividing the integrated peak area by the total detected/identified peak area. All well-defined peaks with at least one percent of the largest peak's height were considered in the calculations.

Table 2.1 is a listing of NIST library results of some of the major peaks in addition to relative area for aspen. The largest peak area belongs to the first peak, which is a combination of water and gaseous species. In addition, this peak grows with increasing temperature from 20% to 53% relative area. Other major contributing peaks that increase with increasing temperature include hydroxyl-acetaldehyde, and 1-hydroxy-2-propanone. Peaks that decrease with increasing temperature include 2-methoxy-phenol, eucalyptol,

29

and 3-hydroxycarbofuran. These trends are in agreement with those discussed previously in section 2.3.3 – that some heavier compounds are further degraded to produce more light material with increasing temperature. Other important contributing peaks include acetic acid, and 3-furaldehyde.

Table 2.1: Peak identification and quantification for aspen.

		Peak Area		
RT (Min)	**Name**	**500**	**600**	**700**
6.2	CO, CO2, H2O	20.0%	38.8%	53.4%
6.7	Propanal, 2,3-dihydroxy-	1.3%		
7.0	Acetaldehyde, hydroxy-	5.7%	7.7%	10.3%
7.6	Acetic acid	3.1%	12.1%	5.2%
7.8	2-Propanone, 1-hydroxy-	9.6%	11.9%	11.9%
9.6	Acetic acid, methyl ester		2.8%	3.0%
10.1	Acetic anhydride	3.1%		2.8%
10.8	3-Furaldehyde	2.3%	3.5%	2.6%
11.4	2-Furanmethanol	1.4%	1.5%	
11.6	1,2-Ethanediol, diacetate	0.3%		
12.8	Cyclopentanone, 2-methyl-			1.7%
13.7	Phenol			1.2%
14.6	2-Cyclopenten-1-one, 2-hydroxy-3-methyl-	1.6%	2.0%	
15.3	Phenol, 3-methyl-			1.1%
15.5	Phenol, 2-methoxy-	2.4%	1.9%	1.4%
16.7	Benzaldehyde, 3-ethoxy-2-hydroxy-	1.1%		
17.0	Phenol, 2-methoxy-4-methyl-	1.9%	1.5%	0.7%
17.4	4H-Pyran-4-one, 5-hydroxy-2-(hydroxymethyl)-	1.4%		
18.4	2,4-Dimethoxytoluene	1.2%	1.0%	
19.4	Eucalyptol	3.6%	2.9%	1.1%
20.9	Phenol, 2-methoxy-4-(1-propenyl)-, (E)-	3.3%	2.3%	1.0%
22.6	3,4-Dimethoxy-5-hydroxybenzaldehyde	1.1%		
23.5	3-Hydroxycarbofuran	6.7%	0.8%	
24.2	à-D-Glucopyranoside, à-D-glucopyranosyl	5.2%		
25.2	Benzaldehyde, 4-hydroxy-3,5-dimethoxy-	1.8%		
		77.9%	90.7%	97.5%

Table 2.2 shows the identifications and peak areas for balsam. Similar to aspen, the combined gas and water peak is the largest and roughly increases with increasing temperature. Some identified compounds that decrease with increasing temperature include 3-furaldehyde, 2-methyl-cyclopentanone, and 2-methoxy-phenol. Comparison with the results for aspen will all note that some of the phenolic compounds, such as 3-methyl-phenol, and 2-methoxy-phenol are present at high concentrations. This can be attributed to the higher concentration of lignin in the original feedstock (26.7% as compared to 36.0%) (Yat et al. 2008). Similarly, the higher number of acetyl compounds found in Table 2.1 can be linked to the higher concentration of xylan in aspen (14.6% as compared to 6.2% in Balsam) (Yat et al. 2008).

Table 2.2: Peak identification and quantification for balsam.

RT (Min)	Name	Peak Area		
		500	600	700
6.2	CO, CO2, H2O	44.5%	49.9%	49.7%
7.0	Acetaldehyde, hydroxy-	10.9%	9.4%	9.9%
7.6	Acetic acid	2.8%	3.8%	2.4%
7.8	2-Propanone, 1-hydroxy-	4.8%	7.3%	3.6%
9.6	Acetic acid, methyl ester	2.2%		1.6%
10.8	3-Furaldehyde	1.7%	1.7%	1.4%
11.4	2-Furanmethanol	1.0%		0.7%
12.8	Cyclopentanone, 2-methyl-	1.9%	1.8%	1.4%
13.7	Phenol			1.1%
14.6	2-Cyclopenten-1-one, 2-hydroxy-3-methyl-	1.2%	1.4%	
15.3	Phenol, 3-methyl-	1.2%	2.0%	2.8%
15.5	Phenol, 2-methoxy-	6.5%	4.8%	2.9%
17.0	Phenol, 2-methoxy-4-methyl-	4.8%	3.7%	2.2%
19.4	Eucalyptol	1.5%	1.4%	1.7%
20.9	Phenol, 2-methoxy-4-(1-propenyl)-, (E)-	2.6%	2.1%	2.7%
		87.5%	89.1%	84.2%

Table 2.3 shows the compound identifications and peak areas for poplar. Similar to the previous feedstocks, the combined gas and water peak is the largest and increases with increasing temperature. Some identified compounds that increase with increasing temperature include acetic acid, and acetic acid methyl ester. Again, many identified compounds are also found in the previous feedstocks.

Table 2.3: Peak identification and quantification for poplar.

RT (Min)	Name	Peak Area		
		500	600	700
1.0	CO, CO2, H2O	12.6%	14.9%	17.3%
1.7	Acetaldehyde, hydroxy-	4.1%	3.3%	4.9%
2.2	Acetic acid	4.4%	4.8%	5.6%
2.5	2-Propanone, 1-hydroxy-	3.9%	3.1%	2.9%
4.8	Acetic acid, methyl ester	1.3%	1.3%	2.7%
5.7	3-Furaldehyde	1.2%	1.3%	1.3%
6.2	2-Furanmethanol	1.2%	1.0%	0.9%
8.6	Phenol		3.5%	2.9%
9.5	2-Cyclopenten-1-one, 2-hydroxy-3-methyl-	1.0%	1.0%	0.9%
10.2	Phenol, 3-methyl-			0.7%
10.4	Phenol, 2-methoxy-	0.9%	1.5%	1.1%
12.1	Phenol, 2-methoxy-4-methyl-	0.9%		1.4%
15.0	Eucalyptol	0.4%	0.7%	4.4%
15.2	Phenol, 2-methoxy-4-(1-propenyl)-	0.1%		
16.0	Phenol, 2-methoxy-4-propyl-	0.2%		
17.1	à-D-Glucopyranoside, à-D-glucopyranosyl	4.5%		
17.6	Phenol, 2-methoxy-4-propyl-	0.4%	0.5%	0.6%
18.3	3-Hydroxycarbofuran	2.9%	3.5%	3.2%
		40.0%	40.4%	47.1%

Table 2.4 shows the identifications and peak areas for red maple. Similar to the previous feedstocks, the combined gas and water peak is the largest peak, but remains approximately constant across the different temperatures. While 2-methoxy-phenol follows the same trends previously noted, it is curious to note that hydroxyl-acetaldehyde and acetic acid both decrease with increasing temperature. This trend is contradictory to some seen previously.

Table 2.4: Peak identification and quantification for red maple.

		Peak Area		
RT (Min)	Name	500	600	700
6.2	CO, CO2, H2O	53.9%	53.2%	53.2%
7.0	Acetaldehyde, hydroxy-	5.2%	2.2%	2.0%
7.6	Acetic acid	6.6%	5.3%	4.8%
7.8	2-Propanone, 1-hydroxy-	8.6%	6.4%	8.2%
9.6	Acetic acid, methyl ester	1.5%	2.3%	1.4%
10.8	3-Furaldehyde	2.4%	2.8%	2.6%
11.4	2-Furanmethanol	1.6%		
12.8	Cyclopentanone, 2-methyl-	2.1%		1.6%
13.7	Phenol			1.2%
14.6	2-Cyclopenten-1-one, 2-hydroxy-3-methyl-	1.5%		1.2%
15.3	Phenol, 3-methyl-		0.9%	1.5%
15.5	Phenol, 2-methoxy-	2.5%	2.3%	1.9%
17.0	Phenol, 2-methoxy-4-methyl-	1.2%	1.2%	0.9%
18.4	Phenol, 2-methoxy-4-propyl-	0.5%	1.0%	1.4%
19.4	Eucalyptol	1.8%	2.5%	2.7%
20.9	Phenol, 2-methoxy-4-(1-propenyl)-, (E)-	0.6%	1.3%	2.2%
23.4	3-Hydroxycarbofuran			0.7%
		90.0%	81.5%	87.2%

Table 2.5 shows the identifications and peak areas for willow. Similar to the previous feedstocks, the combined gas and water peak is the largest and roughly increases with increasing temperature. There are several trends that are very similar to those for poplar including decreasing 1-hydroxy-2-propanone, and 2-furanmethanol, and increasing eucalyptol. Gaseous product peak areas are low compared to other bio-oil components.

Table 2.5: Peak identification and quantification for willow.

		Peak Area		
RT (Min)	Name	500	600	700
1.2	CO, CO2, H2O	11.4%	14.1%	13.9%
1.7	Acetaldehyde, hydroxy-	3.9%	3.6%	4.8%
2.4	Acetic acid	3.7%	3.6%	3.5%
2.5	2-Propanone, 1-hydroxy-	4.2%	2.6%	1.8%
4.9	Acetic acid, methyl ester	0.8%	1.4%	1.5%
5.7	3-Furaldehyde	1.5%	1.5%	1.2%
6.2	2-Furanmethanol	1.0%	0.9%	0.7%
7.6	Cyclopentanone, 2-methyl-	2.1%	2.4%	1.7%
8.7	Phenol	0.8%	1.4%	1.0%
9.5	2-Cyclopenten-1-one, 2-hydroxy-3-methyl-	0.8%	1.0%	0.7%
9.9	Phenol, 3-methyl-	0.2%	1.5%	2.0%
10.5	Phenol, 2-methoxy-	1.1%	1.8%	1.5%
12.1	Phenol, 2-methoxy-4-methyl-	1.4%	2.1%	1.8%
14.4	Eucalyptol	5.7%	6.0%	6.3%
15.18	Phenol, 2-methoxy-4-(1-propenyl)-, (E)-	0.3%	0.3%	
17.85	à-D-Glucopyranoside, à-D-glucopyranosyl		1.5%	
18.5	3-Hydroxycarbofuran	7.5%	5.3%	10.3%
		46.3%	50.9%	52.5%

Table 2.6 shows the peak identification matches for switchgrass. As before, the largest peak contribution is due to the water and gaseous species peak. Again, trends are hard to indentify for this feedstock. With increasing temperature, 2-methoxy-phenol is decreasing, 3-furaldehyde is roughly decreasing, eucalyptol is increasing.

Table 2.6: Peak identification and quantification for switchgrass.

		Peak Area		
RT (Min)	Name	500	600	700
6.2	CO, CO2, H2O	50.6%	54.1%	49.3%
7.0	Acetaldehyde, hydroxy-	2.1%	1.6%	1.7%
7.6	Acetic acid	6.8%	7.4%	6.1%
7.8	2-Propanone, 1-hydroxy-	8.3%	6.7%	8.0%
9.6	Acetic acid, methyl ester	1.6%		1.4%
10.8	3-Furaldehyde	2.7%	2.9%	2.2%
12.8	Cyclopentanone, 2-methyl-	1.5%	0.6%	
13.7	Phenol			2.5%
14.6	2-Cyclopenten-1-one, 2-hydroxy-3-methyl-	2.0%	1.6%	1.9%
15.3	Phenol, 3-methyl-	1.8%	1.2%	2.6%
15.5	Phenol, 2-methoxy-	3.6%	2.9%	2.6%
17.0	Phenol, 2-methoxy-4-methyl-	0.9%	0.8%	0.9%
19.4	Eucalyptol	0.9%	0.9%	1.4%
20.9	Phenol, 2-methoxy-4-(1-propenyl)-, (E)-	0.5%	0.6%	0.8%
		83.3%	81.1%	81.4%

2.4 Conclusions

The pyrolysis experiments carried out in this work shows a similar trend as in the literature for fast pyrolysis in that gaseous and liquid products increase with increasing pyrolysis temperature. The char fraction does, however, decrease with increasing temperature consistent with literature. In addition, gaseous phase pyrolysis products increase with increasing temperature (the volume and rate of gas production increase with temperature). The largest gas species present was usually CO_2, but CO was the preferred gas product at higher temperatures for some feedstocks. This work also demonstrated

that the major products from wood pyrolysis are a mixture of syngas, light oxygenated species - such as organic acids, aldehydes, and esters – and heavier phenol-based compounds. Depending on the feedstock species and pyrolysis temperature, 10-55% of the detectable area is devoted to water and syngas, 2-12% to acetic acid, 2-12% to hydroxypropanone, 1-3% to furaldehyde, and 5-15% to various phenolic compounds. These results are similar to the combination of pure cellulose, hemicelluloses, and lignin results, and act to supplement existing literature.

3 Kinetic Study of Aspen during Torrefaction

3.1 Introduction

In addition to using biomass to produce biofuels or intermediates, it can also be utilized in electricity generation systems. It is expected that electricity production by coal-fired utility boilers will continue to be stable at ~45% of total production in the next 30 years (EIA 2009; 2010). Co-firing raw-biomass in coal-fired boilers had been attempted for demonstration and commercial purposes (Reichling and Kulacki 2011). In fact, direct combustion of raw-biomass initially seemed the most promising solution to reduce greenhouse gases in electricity generation systems (Ayhan 2008). Some problems encountered, however, such as the high cost and emissions of grinding raw-biomass, high bulk volume, moisture content, low calorific value, hydrophobicity of the material, thermal instability, and production of undesired tars (Devi et al. 2003; Bergman 2005; Prins et al. 2007). One possible solution to address these issues while still utilizing biomass is the use of torrifaction.

Biomass torrefaction is a mild thermal treatment in absence of oxygen at the 200-300°C, and is a coupled chemical-kinetic-heat-and-mass-transfer process. Torrefied biomass (bio-coal) has properties similar to coal, while maintain the greenhouse gas benefits. In real electricity generation systems, whether they are pulverized coal boiler systems, combined heat and power systems, or gasification systems, a key aspect is their high throughput and processing rate of feedstock material (Spath et al. 1999; Reichling and Kulacki 2011). These high-volume systems create the necessity for an accurate understanding of the major processing stages.

A recent review article by Chew and Doshi (Chew and Doshi 2011) contains a summary of proposed kinetic mechanisms for wood torrefaction. These models include a single step global model (Repellin et al. 2010), a three parallel reaction model (Shafizadeh and Chin model), two step consecutive model (Di Blasi–Lanzetta model) (Prins et al. 2006; Repellin et al. 2010), and a two parallel reaction model (Broido–Shafizadeh model) (Repellin et al. 2010). These models, however, were studied with the use or TGA, or

TGA-like conditions. Although torrefaction has been investigated for some time, literature has been focused around TGA (Chen and Kuo 2011; Chew and Doshi 2011) studies without yielding true mechanistic insights for real industrial situations – fast heating rate torrefaction.

3.1.1 Improvements with Torrefied Biomass

Torrefied-biomass can be considered a premium biofuel with properties similar to coal, requiring no added technological upgrades to utility boilers such as large capital investments, or high operation costs; therefore, it can be utilized as a "drop-in" fuel for coal. The largest, and most notable improvement of bio-coal over raw biomass is the reduction of energy required for size reduction to a pulverized state. The amount of energy required to reduce the size of feedstock particles is reduced by more than ten times for biocoal compared to untreated woody biomass (Bergman 2005). During torrefaction, hemicelluloses decompose and change the viscoelastic properties of the biomass, improving the biomass grindability (Panshin and deZeeuw 1980). It addition to the decrease in size reduction costs, torrefaction was found to increase the calorific value of woody feedstocks by 40%, though the mass was reduced by 50% (Chen et al. 2011).

3.1.2 Research Objectives

The discussion above implies that existing literature on coal electricity generation systems, or rather preparation of biomass for bio-coal electricity generation systems, has been focused on insights derived from TGA studies. While these studies have merit in their own right, TGA analyses are usually carried out between 5 and 15˚C/min whereas heating rates in industrial applications would be much higher. The difference in heating rates can yield very different proposed mechanisms. The objective of this research is to propose simple mechanistic models for biomass torrefaction with fast heating rates and to compare these models to measurements of products from torrefaction, CO_2 and acetic acid, over time. Also, suggestions for improvement of the models will be noted.

3.2 Materials and Methods

3.2.1 Experimental Equipment

The experimental equipment used in this chapter is identical to section 2.2.1.

3.2.2 Biomass Preparation

The biomass used for these experiments was aspen. The biomass samples used in this chapter were prepared identically to section 2.2.2.

3.2.3 Direct Torrefaction-GC/MS Experiment

The torrefaction experiments were performed similar to those described in section 2.2.4. Again, fast heating rates (999˚C/sec) were used along with sample sizes around 0.5-1.0 mg. In these experiments, however, torrefaction processing temperatures were used (300°C instead of 500-700°C) and held for much longer times (>30min instead of 15 seconds). In addition, the GC column was not heated. This provides time dependent analysis for the light slightly-adsorbable species only. Here the data analysis involves tracking an ion fragment's detection intensity over time. These transients are demonstrated in Figure 3.1. This temporal history yields direct insight as to when the parent compound formed from the heated sample.

To eliminate GC/MS effects, including the time delay between species evolution at the biomass sample and the arrival of the species at the MS detector and to test the validity of the temporal history, several 'pulse inputs' were performed while their response was recorded. These inputs were very brief (5 second) period of torrefaction. To ensure an accurate history the response of the detector, the MS in this case, should be as close to the input as possible. Figures 3.2 and 3.3 show these responses.

3.3 Results and Discussion

When examining the results from the torrefaction experiments, at least two different distinct groups of products are formed. The first group to evolve from the sample consists of gases (CO, CO_2) and water. The second group contains organic acids (acetic acid, formic acid). This group differentiation is shown in Figure 3.1.
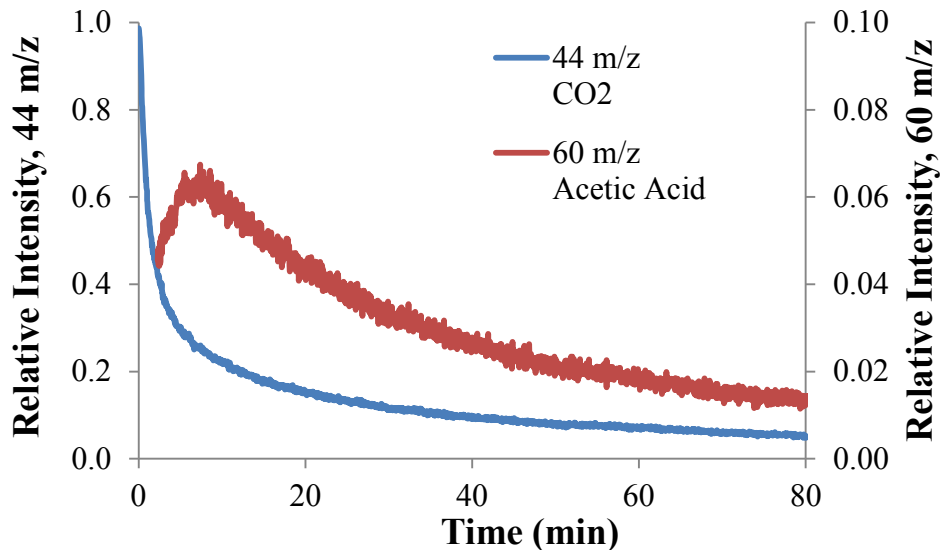
**Figure 3.1: Mass spectra transient for acetic acid and carbon dioxide during torrefaction of aspen**

Figure 3.1 shows the relative MS intensities for ion fragments 44m/z and 60m/z (fragments of CO_2 and CH_3COOH respectively) over time during 300°C torrefaction of aspen. These MS intensities (signal height) are normalized by the maximum intensity of the larger signal, CO_2 and the time axis was adjusted to account for the time delays discussed in section 3.2.3. The acetic acid trace does not trend down to zero intensity at t = 0 after time time axis adjustment, but maintains at a relatively high intensity (about .04) at slightly negative times. We believe that this is caused by GC column overloading by the acetic acid resulting in early arrival compared to the pulse-response experiment. Nonetheless, it is clear from these two ion traces that they appear to evolve from the sample at different times. Because of the delayed formation of acetic acid relative to CO_2, it is proposed that the best and easiest way to describe this behavior is with a series

of sequential reactions. This type of model should allow for the evolution of CO_2 and its' related compounds at earlier times, and explain why acetic acid and its' related compound are not formed in any significant quantities until after the sample materials have degraded.

3.3.1 Input-Response Validation

There are several factors that affect the comparison between the temperature input to start an experiment, and the MS signal intensity repose that is measured. The first impact is due to heat transport limitations. Although the samples (particle size and mass) are small to minimize this effect, there is still an unavoidable and inherent deviation between the temperature of the sample probe, the surface of the sample, and the core of the sample. The second impact is due to column interactions. Again, these effects should be small as the materials are not perfectly retained by the column at room temperature. The final complication can be attributed to flow dispersion effects. Using the physical properties of helium at ambient conditions and a GC constant gas flow of 1.5 mL/min (superficial velocity of 50.93 cm/sec), the flow was determined to be fully laminar with a Reynolds number of 1.22. Because of this, the dispersion effects can be described, at least partly, by Taylor dispersion.

Figure 3.2 shows the input-response behavior for the 44 m/z ion fragment over time. This fragment can be attributed to carbon dioxide. After the 5 second heating of sample that occurs at time t = 300 seconds, the MS begins to record a response around time t = 365 seconds. This response shows very fast decrease in mass detection, and some peak broadening due to dispersion effects and interactions with the GC column. Starting at time t = 365 seconds, the signal reaches peak apex after 7 seconds, has decreased to approximately 50% intensity after 10 seconds, and is almost entirely gone after 20 seconds have passed. This quick response demonstrates minor impacts due to interactions with the column and dispersion. Because CO_2 is non-polar there are smaller interactions between the gas and the column when compared to acetic acid. This implies that the observed impacts might be more attributable to flow dispersion. The response shown in Figure 3.2 was compared with general Taylor dispersion solutions
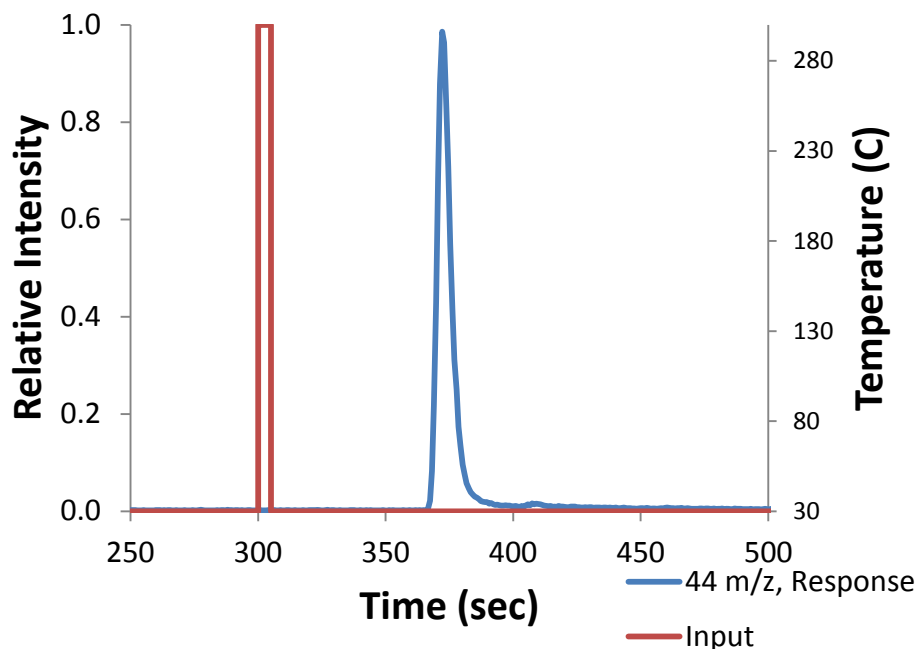
Figure 3.2: Input-response diagram for CO$_2$ (44 m/z)

(Bird et al. 2007), and is presented in Appendix E.   From this analysis in Appendix E it was concluded that Taylor dispersion cannot entirely explain the dynamics of the signal response, and other factors should be investigated, such as column interaction.

Figure 3.3 shows the input-response behavior for the 60 m/z ion fragment over time. This fragment can be attributed to acetic acid (CH$_3$COOH). After the 5 second heating of sample that occurs at time t = 300 seconds, the MS begins to record the true formation response around time t = 405 seconds.   This response shows a slower decrease than the 44m/z trace, but still fairly quick decrease in mass detection. Starting at time t = 405 seconds, the signal reaches peak apex after an additional 4 seconds, has decreased to approximately 50% intensity after 7 seconds, and is almost entirely gone after 60 seconds have passed.   The response behavior with regard to the 60m/z fragment appears to deviate from the 44m/z fragment after the intensity has decreased to approximately 40% of the apex.   At this point, the response peak broadens greatly and takes a relatively longer amount of time for the signal to dissipate.   This delayed dissipation is mostly likely due to acetic acid's polarity, and interaction with the column.   Overall, the response deviation is likely a combination of dispersion and column interaction effects.
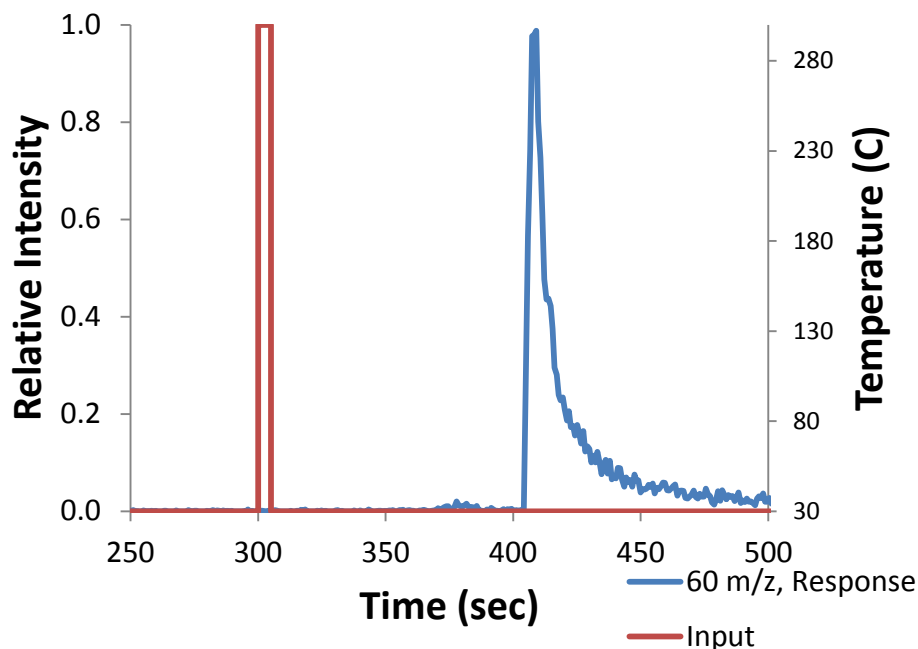
Figure 3.3: Input-response diagram for acetic acid (60 m/z)

3.3.2 Kinetic Models and Interpretation

Even with the identified complications, a preliminary attempt was made to model torrefaction kinetics with three simplifying assumptions. First, it was assumed that there is instantaneous heating within the sample. This neglects complications associated with heat transport limitations. The second assumption is that the interactions with the column resin are negligible. The final assumption was that the dispersion due to flow through the column is represented by Taylor dispersion (due to laminar flow) and is of minor contribution. The latter two assumptions can justified in comparing the delay within the pulse inputs (manifested within approximately 1 minute), and the actual species formations (manifested over several 10s of minutes).   Within the input-response diagrams, there is approximately a 40 second delay between signal observation between the CO_2 and acetic acid.   Within the experiment, it was observed that there was approximately 10 minutes between maximum species formation.   Although these contributions can have a significant contribution and complicate the results, the system was simplified for the purposes of this work.

In order to analyze the data and fit the kinetic rate constants appropriately, the experimental data was evaluated "at the sample." Before the sample began to heat within the experiment, the GC/MS recorded data for 25 minutes to establish a consistent baseline. This delay before the sample began to heat was taken into consideration by converting the original time = 25 minutes point to the new time = 0 minutes point. An additional time shift was performed to take into account the results from the input-response trials by way of incorporating the delay from the start of the impulse to the apex of the response. This would translate the time axis to represent the true time transient of evolution at the sample. The original experimental delay (the 25 minutes before the sample began heating) also allowed for removal of signal bias. This bias comes from the MS detector recording signal, when nothing is present in the system. By making a linear fit to the signal observed in the delay (nothing in the system), the detector bias was removed over the entire experiment. Finally, both species intensities were normalized by the CO_2 maximum intensity.

The formation of the first group of products, represented by CO_2 in Figure 3.1, appear to decrease exponentially, but is more likely comprised of multiple exponential functions. Because of this and reasons previously mentioned the first proposed mechanism consists of two first order reactions where P_1, or CO_2 and related materials, are formed through a primary and secondary reaction, and P_2, or acetic acid and related materials, are formed purely through a secondary series reaction:

$$R_1 \xrightarrow{k_1} R_2 + P_1 \tag{2}$$

$$R_2 \xrightarrow{k_2} P_1 + P_2 \tag{3}$$

where R_1 is the original parent material (hemicelluloses or xylan-chains), R_2 is a reaction intermediate, P_1 is the gaseous species and water, P_2 is the organic acid species, and k_1 and k_2 are reaction rate constants.

These reactions yield the following expressions for concentrations as a function of time, assuming constant temperature such that k_1 and k_2 are constant.

$$R_1 = (R_1)_o e^{-k_1 t} \tag{4}$$

$$R_2 = (R_1)_o \frac{k_1}{k_1 - k_2} (e^{-k_2 t} - e^{-k_1 t}) \tag{5}$$

$$\frac{dP_1}{dt} = k_1 (R_1)_o e^{-k_1 t} + \varepsilon (e^{-k_2 t} - e^{-k_1 t}) \tag{6}$$

$$\frac{dP_2}{dt} = \varepsilon (e^{-k_2 t} - e^{-k_1 t}) \tag{7}$$

Where the constant

$$\varepsilon = (R_1)_o \frac{k_1 k_2}{k_1 - k_2} \tag{8}$$

Derivation of these solutions is attached as Appendix C. The solutions for the product concentrations as a function of time were then fit to experimental data by minimizing the squared error between the data and the model's predicted values. The error of the P2 species model was scaled to reflect differences in relative intensities (approximately 15:1) between species. This was done in an effort to fit the models simultaneously with equal weighting between all points in both species. The number of data points was reduced by a factor of 10 by averaging the MS signal for every subsequent 10 data points in the time series. Initial parent concentration, $(R_1)_o$, is system/experiment dependent and thus arbitrary. The reaction rate coefficients, however, were found to be $k_1 = 0.3441$ min^{-1} and $k_2 = 0.0257$ min^{-1}. Interpreting the characteristic time loosely as the inverse reaction rate, the characteristic times are approximately 2.9 min and 38.9 min respectively. The two series reaction model is shown in Figure 3.4.

This model, as seen in Figure 3.4, seems to fit P2 well. It does, however, underpredict P1 at large times. This difference suggests that the addition of a third reaction, parallel to the second reaction in the series, might fit the data better to accommodate the behavior of P1.

45
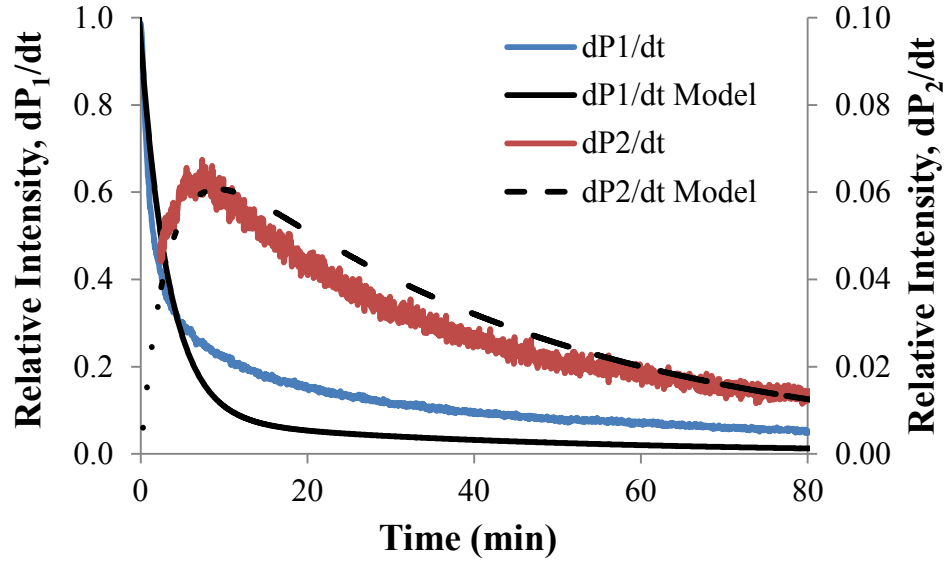
Figure 3.4: Experimental data with two-series reaction mechanism model

Another reaction very similar to the second reaction above was used as a starting point of further model investigation. In this addition reaction the intermediate reactant material R_2 is further degraded to some additional intermediate R_3 via rate constant k_3 which, in-turn, is degraded to yield more of the product classes.

The three series reaction model can be summarized as:

$$R_1 \overset{k_1}{\to} R_2 + P_1 \tag{9}$$

$$R_2 \overset{k_2}{\to} R_3 + P_1 + P_2 \tag{10}$$

$$R_3 \overset{k_3}{\to} P_1 + P_2 \tag{11}$$

where R_1 is the original parent material (hemicelluloses or xylan-chains), R_2 and R_3 are reaction intermediates, P_1 is the gaseous species and water, P_2 is the organic acid species, and k_1, k_2, and k_3 are reaction rate constants.

46

These reactions yield the following expressions for concentrations as a function of time:

$$R_1 = (R_1)_o e^{-k_1 t} \tag{12}$$

$$R_2 = (R_1)_o \frac{k_1}{k_1 - k_2} (e^{-k_2 t} - e^{-k_1 t}) \tag{13}$$

$$R_3 = \delta (R_1)_o [(k_2 - k_3)(e^{-k_1 t} - e^{-k_3 t}) + (k_1 - k_3)(e^{-k_3 t} - e^{-k_2 t})] \tag{14}$$

$$\frac{1}{(R_1)_o} \frac{dP_1}{dt} = (k_1 + \alpha) e^{-k_1 t} + \beta e^{-k_2 t} + \gamma e^{-k_3 t} \tag{15}$$

$$\frac{1}{(R_1)_o} \frac{dP_2}{dt} = \alpha e^{-k_1 t} + \beta e^{-k_2 t} + \gamma e^{-k_3 t} \tag{16}$$

With constants

$$\alpha = \frac{k_1 k_2 k_3}{(k_1 - k_2)(k_1 - k_3)} - \frac{k_1 k_2}{k_1 - k_2} \tag{17}$$

$$\beta = \frac{k_1 k_2}{k_1 - k_2} - \frac{k_1 k_2 k_3}{(k_1 - k_2)(k_2 - k_3)} \tag{18}$$

$$\gamma = \frac{k_1 k_2 k_3}{(k_1 - k_2)(k_2 - k_3)} - \frac{k_1 k_2 k_3}{(k_1 - k_2)(k_1 - k_3)} \tag{19}$$

$$\delta = \frac{k_1 k_2}{(k_1 - k_2)(k_1 - k_3)(k_2 - k_3)} \tag{20}$$

Derivation of these solutions is attached as Appendix D. As with the first mechanistic model, the solutions for the product concentrations as a function of time were then fit to experimental data. This new three-series reaction model is shown in Figure 3.5.

The 3-series reaction model appears to capture the reaction characteristics for P2 well, as seen in Figure 3.5. Similarly to the previous model, the formation of P_1 appears to be modeled well at early times, but is underestimated at longer times. The similarities between the solution for this model and the two-reaction model demonstrate that the mechanism is more complicated, and needs further refinement.
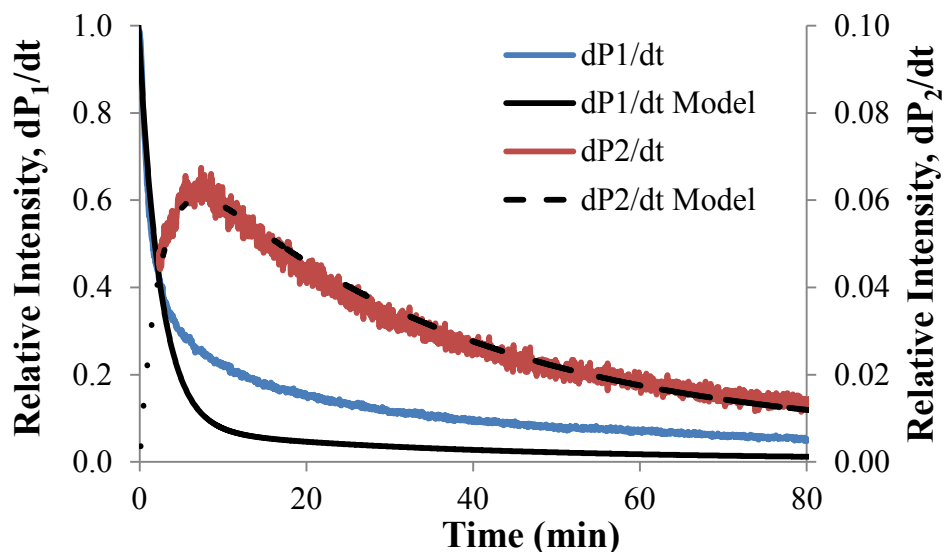
Figure 3.5: Experimental data with three-series reaction mechanism model

As with the two-series reaction model, the initial parent concentration, $(R_1)_o$, is system/experiment dependent and therefore arbitrary to a mechanistic model. With the three-series model, the reaction rate coefficients were found to be 0.396 min^{-1}, 0.031 min^{-1}, and 0.003 min^{-1} for k_1, k_2, and k_3 respectively. Interpreting the characteristic time as the inverse reaction rate, the characteristic times are approximately 2.5 min, 32.8 min, and 385.4 min, respectively. Because two of these characteristic times occur early, it is implied that there is a more complex behavior at early times in the reaction, which settles to a simple decay at the later reaction times. This could direct future work at further investigation of the early torrefaction time points, and perhaps merit a more complex model.

The closest literature match to this proposed mechanism is the two-step consecutive Di Blasi–Lanzetta model mentioned previously (Prins et al. 2006). This model interpreted by Prins used willow as a feedstock and isothermal TGA experiments (10˚K/min heating). Using the temperature dependent solutions for the rate expressions presented, the rate coefficients were found to be k_{v1} = 0.075 min, and k_{v2} = 0.014 min respectively, leading to characteristic times of 13.3min and 70.7min for a temperature of 300˚C. These values for rate constants are not radically different from those found above, and share the

behavior of having a relatively quick reaction, followed by a much slower one. The proposed reaction scheme was:

$$A \xrightarrow{k_{v1}} V_1 \ , \ \ A \xrightarrow{k_1} B \tag{20}$$

$$B \xrightarrow{k_{v2}} V_2 \ , \ \ B \xrightarrow{k_2} C \tag{21}$$

where A is the parent biomass, B is a reaction intermediate, C is the solid product, V_1 and V_2 are volatile product groups, and k_1, k_2, k_{v1}, and k_{v2} are reaction rate constants.

3.4 Conclusions

Two models were developed within this work to describe the evolution of light-weight, non-condensable and condensable species formed during torrefaction of aspen. The evolution of these products yielded insight into mechanistic changes that the biomass undergoes during torrefaction. It was observed that gaseous species, such as CO_2, evolve from the biomass sample very quickly, and are followed by the gradual evolution of organic acids, such as acetic acid. From this behavior, a two-reaction series and three-reaction series model were proposed to describe the system. Both models yielded similar results, modeling acetic acid formation well, but under-predicting CO_2 production at long times. The two-reaction series model predicts characteristic times of 2.9 min and 38.9 min for the reactions, and the three-reaction series model predicts characteristic times of 2.5 min, 32.8 min, and 385.4 min for the reactions.

The under prediction of gaseous species such as CO_2 at large times suggests that a modification to the model mechanism might improve the fit to the data. One modification to the model that might fit the data better would be a parallel reaction for production of gaseous product, P_1, from the intermediate product R_2. This and other model refinements will be explored in future research. Another possible improvement of the model is to generate more accurate experimental data. One improvement should involve the use of a short and inert GC column so that there is very little time delay between species evolution at the micropyrolysis sample and very little interaction with the GC column material. These experiment improvements will be explored in future research.

4 Improvements in Pyrolysis Processing with Torrefaction as a Pre-Treatment

4.1 Introduction

The production of biofuels from biomass gained accelerated interest as these fuels are potentially economically-viable, renewable, and carbon-neutral energy sources. Yet, many barriers have been encountered when using raw biomass in pyrolysis for the production of bio-oils. These problems have produced the need to upgrade biomass prior to producing a high-grade bio-oil. Preliminary work has been done in this research to investigate torrefaction as a possible pretreatment that would improve the properties the resulting pyrolysis-oil.

4.1.1 Disadvantages of Pure Pyrolysis Oil

Several elemental analyses have shown that bio-oil contain between 45% and 50% bound oxygen, 55-60% carbon, and small amounts of hydrogen, nitrogen, and ash (Bridgwater et al. 1999; Mohan et al. 2006). Bio-oil produced prom fast pyrolysis contains large amounts of: (1) acids, causing severe high temperature corrosion and degrading the bio-oil during storage; (2) bound oxygen, imposing challenges in the catalytic hydrotreatment processes; and (3) water that decreases the quality of the bio-oil. All these are evident problems when attempting to upgrade the bio-oil to transportation fuels.

4.1.2 Torrefaction as a Biomass Pretreatment Before Pyrolysis

As discussed previously, biomass torrefaction is a mild thermal treatment in absence of oxygen at the 200-300°C temperature range and is traditionally used to convert wood into char-coal for domestic and some limited industrial applications. Investigations into biomass torrefaction yielded the following behavior:

1. Hemicelluloses almost exclusively degrades in this temperature range (Yang et al. 2007)
2. Water, CO, CO_2, organic acids are major products (Klinger et al. 2011)
3. Acetic acid is not produced by cellulose and lignin (Klinger et al. 2011)
4. Biocoal properties can be tightly controlled, thus reducing significantly the variability in the feedstock (Bar-Ziv and Chudnovsky 2011)

Because of these observations, torrefaction was investigated to improve the quality of the produced fast pyrolysis oils.

## 4.2 Materials and Methods

4.2.1 Experimental Equipment

The experimental equipment used in this chapter is identical to section 2.2.1.

4.2.2 Biomass Preparation

The biomass used for these experiments was aspen. The biomass samples used in this chapter were prepared identically to section 2.2.2.

4.2.3 2-Stage Torrefaction-Pyrolysis Experiment

The 2-stage pyrolysis-torrefaction experiments were performed similar to those described in section 2.2.4. Again, fast heating rates were used along with sample sizes around 0.5-1.0 mg. In these experiments, however, there are three distinct heating stages: the first is for drying the moisture in the biomass sample (at 120°C), the second is for torrefaction (at 300°C), and the third for pyrolysis (at 600 $^{\circ}$C). The length of time for the first stage depends on the quantity of moisture in the sample, the second stage depends on torrefaction temperature and biomass characteristics, and the third stage can usually be completed very quickly, depending on biomass characteristics and particle sizes (particles from 500-600 microns were used again here). Figure 4.1 shows these consecutive heating/experimental stages as they were performed.
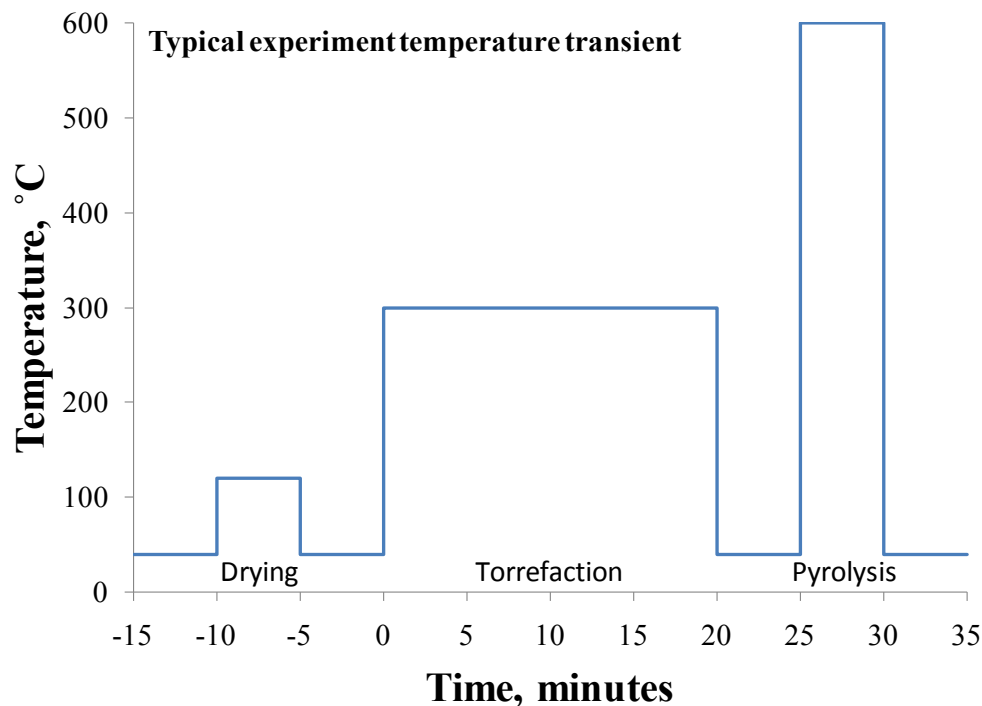
Figure 4.1: Typical two-stage experimental temperature transient

When interpreting and analyzing the data, two different methods were used. In the first method, the entire mass spectra was considered at a given time point. From a given spectra of ion fragments, the chromatogram peaks were identified by comparing them against a database available from the National Institute of Standards and Technology (NIST). This was primarily used in identifying the condensable compounds that would reside in the resulting bio-oil. In the second method only one ion fragment value (ie: 60 m/z) was considered, but over the entire experimental time. From this data, the intensity of the given ion fragment was quantified and tracked over the various experimental stages. This method was used in determining inhibitory compound reduction (e.g. acetic acid) between single stage pyrolysis and two stage torrefaction-pyrolysis, and compound behavior analysis.

The GC-MS was operated to enable the direct measure of the "light", non-condensable, components (H_2O, CO, CO_2, CH_3OH, and CH_3COOH, and some aldehydes) as well as the condensable species forming the bio-oil; this was done by: (1) first without heating

the separation column thus providing on-line, real-time, temporal history of these "light" non-condensable gases; because these "light" species do not condense on the chromatograph column at room temperature and they are immediately monitored by the MS, and (2) heating of the chromatographic column at a rate to enable the separation and identification (through retention time and mass spectrum) of the various liquid components was carried out. Mass intensity transients were obtained by the system software.

4.3 Results and Discussion

Figures 4.2 - 4.5 show mass spectra signal vs. chromatographic retention time for some of the non-condensable components released from aspen wood during torrefaction. Torrefaction time and temperature was 30 minutes and 300°C, respectively. To validate that masses 17 and 18 belong to water their mass transient signals were normalized by their maximum MS signal, shown in the inset of Figure 4.2 that provided identical behavior. The same was carried out for masses 43, 45, and 60, validating that these belong to acetic acid in Figure 4.5.

Because the sample were dried prior to conducting the torrefaction-pyrolysis experiments, the results from Figure 4.2 has shown that water is being removed through dehydration reactions. In addition, Figure 4.5 demonstrates that torrefaction is indeed removing acetic acid.
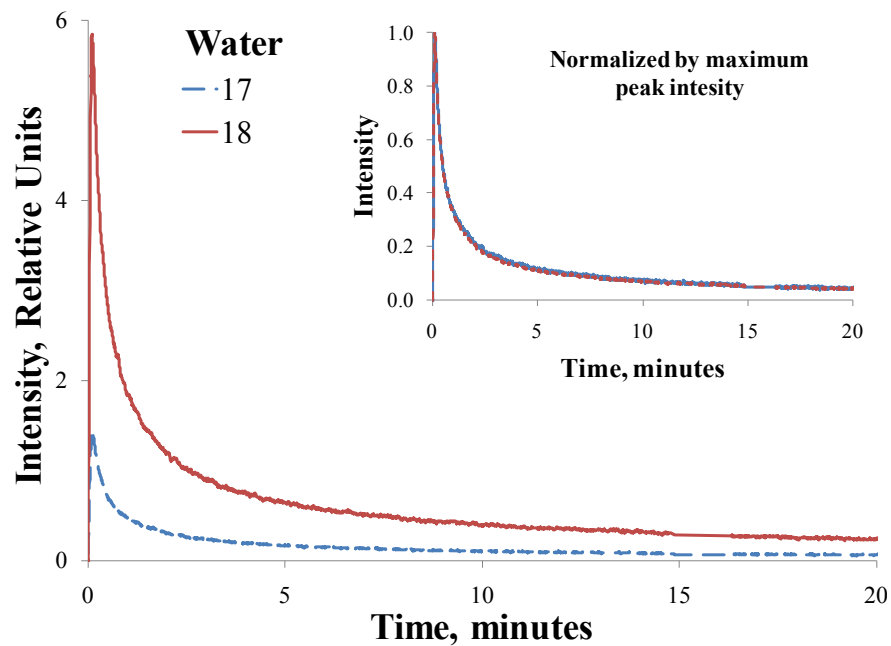
Figure 4.2: **Mass spectra transient for water (17 and 18 m/z) during torrefaction of aspen.**
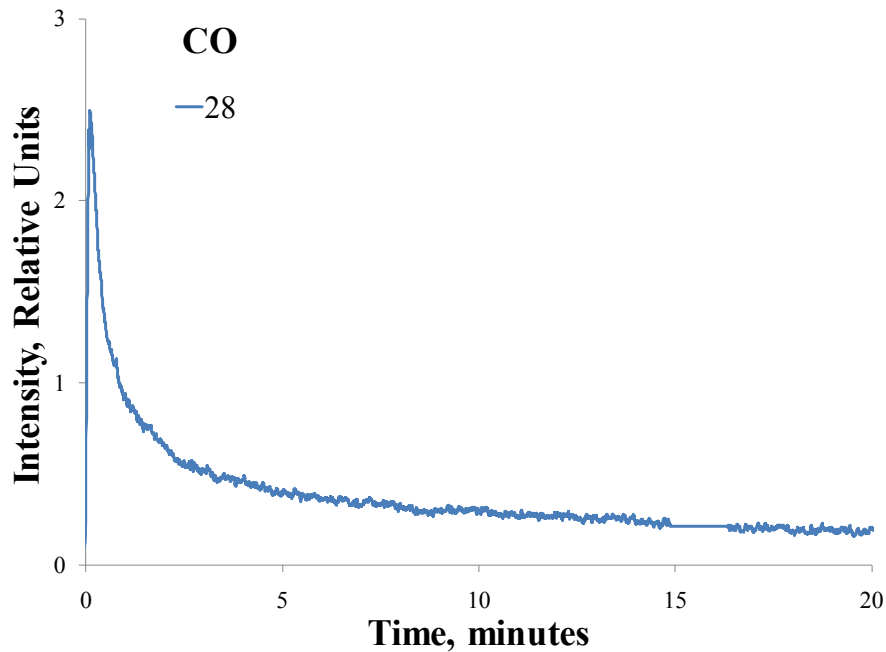
Figure 4.3: Mass spectra transient for carbon monoxide (28 m/z) during torrefaction of aspen.
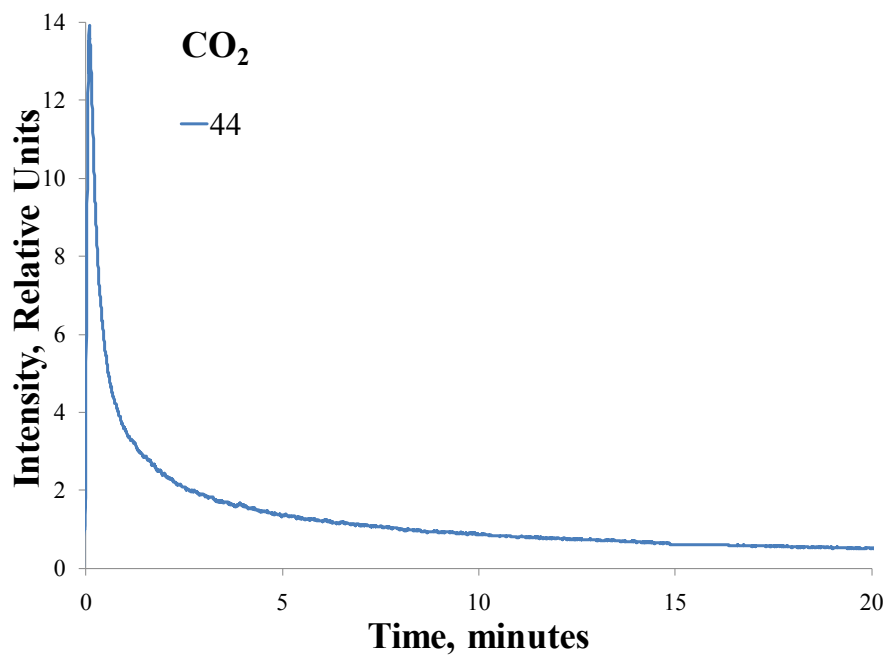
Figure 4.4: Mass spectra transient for carbon dioxide (44 m/z) during torrefaction of aspen.
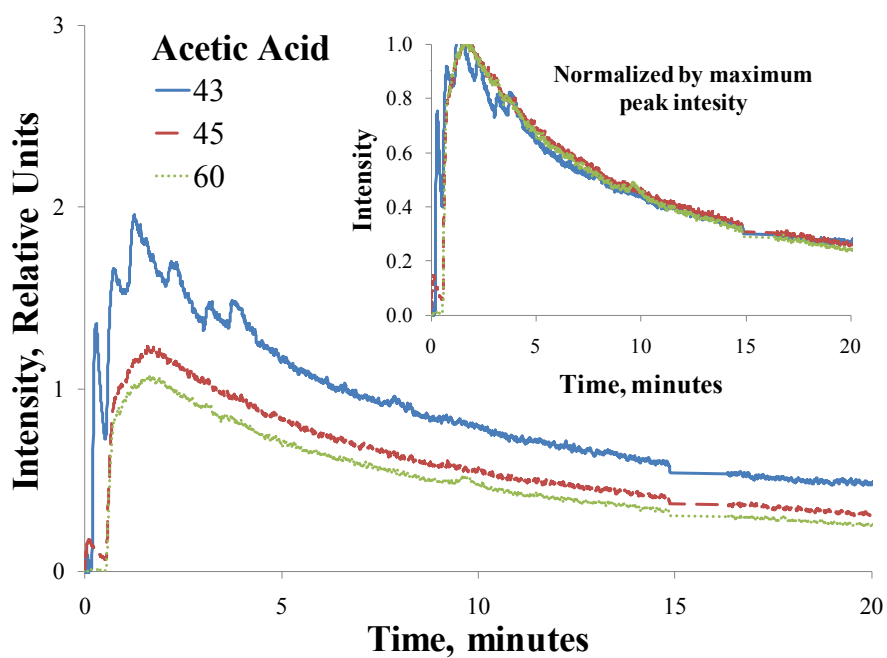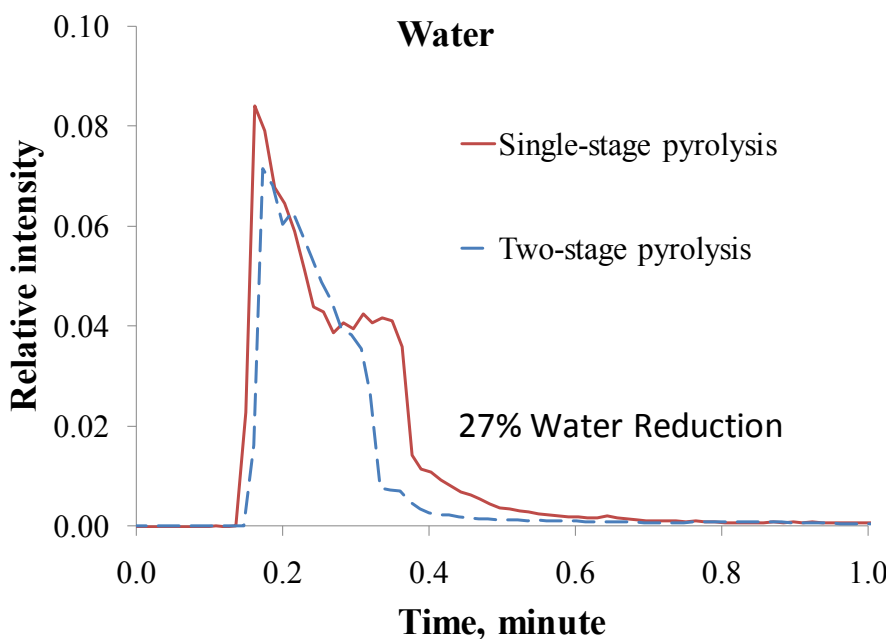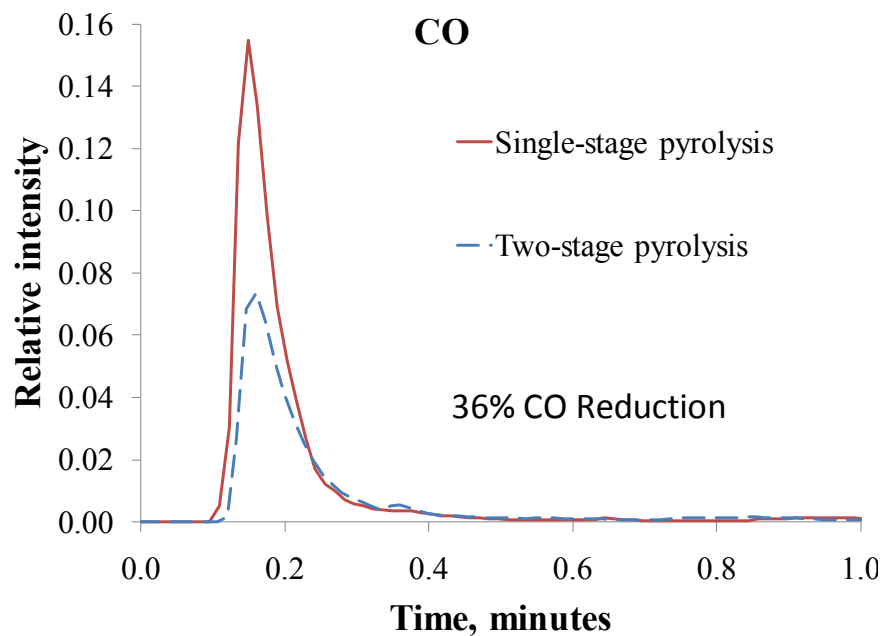

Figure 4.5:   Mass spectra transient for acetic acid (43, 45 and 60 m/z) during torrefaction of aspen.

The results provide quantitative measure of the reduction of the undesired components we wish to avoid in the pyrolysis stage. In order to get this information, the integral of each of these components was taken from the two stages – torrefaction and pyrolysis. The components' reduction (compared to traditional pyrolysis) due to torrefaction were calculated to be 27%, 36%, 55%, and 67% for water, CO, CO_2, and acetic acid respectively. The most impressive and important reduction is acetic acid. These comparisons are shown as Figures 4.6-4.9.

Figures 4.10 and 4.11 show chromatograms for the heavy-weight (bio-oil) species from single-stage and two-stage fast pyrolysis respectively. As can be observed, there is a great difference between the product distributions in the two pyrolysis processes. In both processes phenols, eucalyptol, and saccharides are present, however, in the single-stage pyrolysis light ketones, furaldehyde, and alcohols are much more prevalent. This would imply that oil produced from the two-stage processing method has lower O/C ratios.
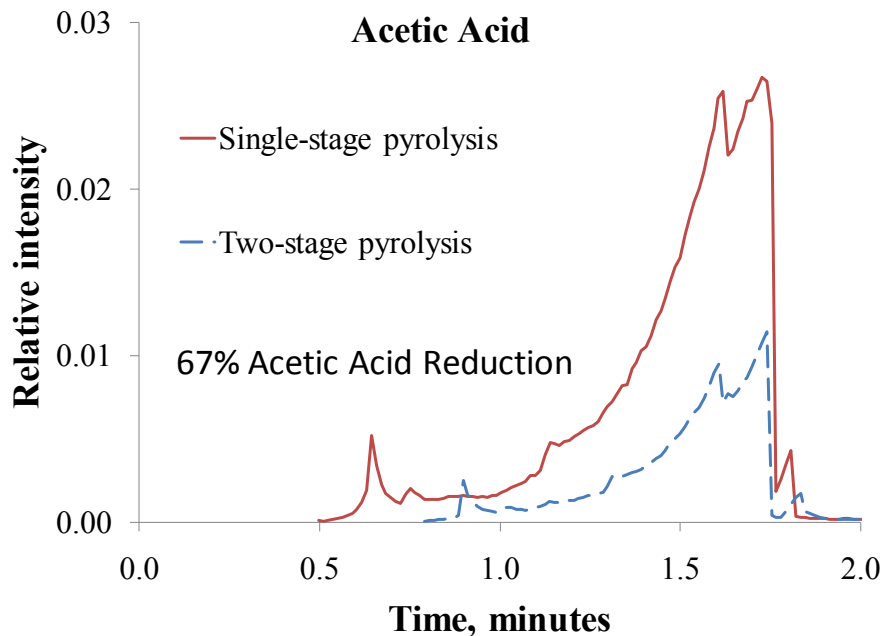

Figure 4.6: Mass spectra transient for water during single-stage and two-stage pyrolysis.

CO

36% CO Reduction

Figure 4.7: Mass spectra transient for carbon monoxide during single-stage and two-stage pyrolysis.
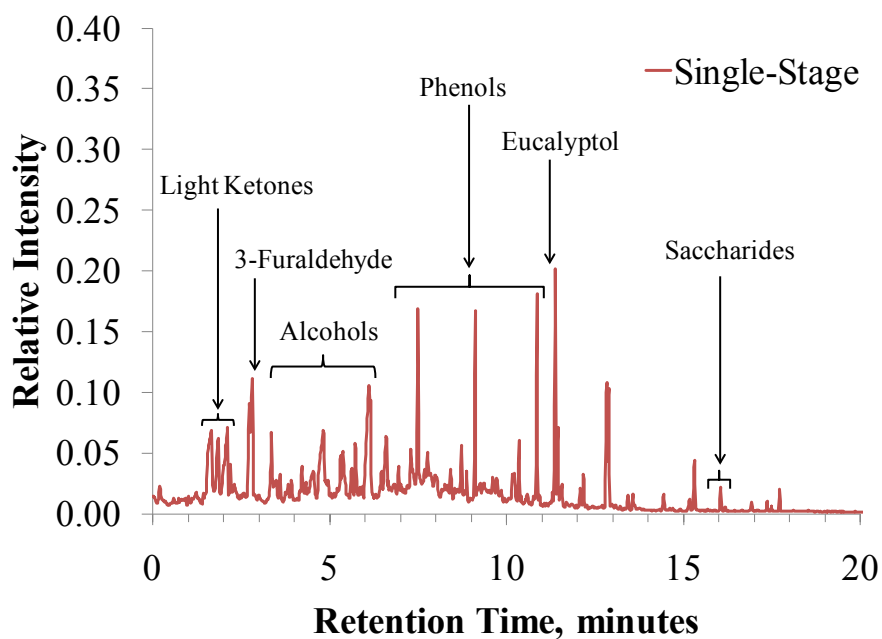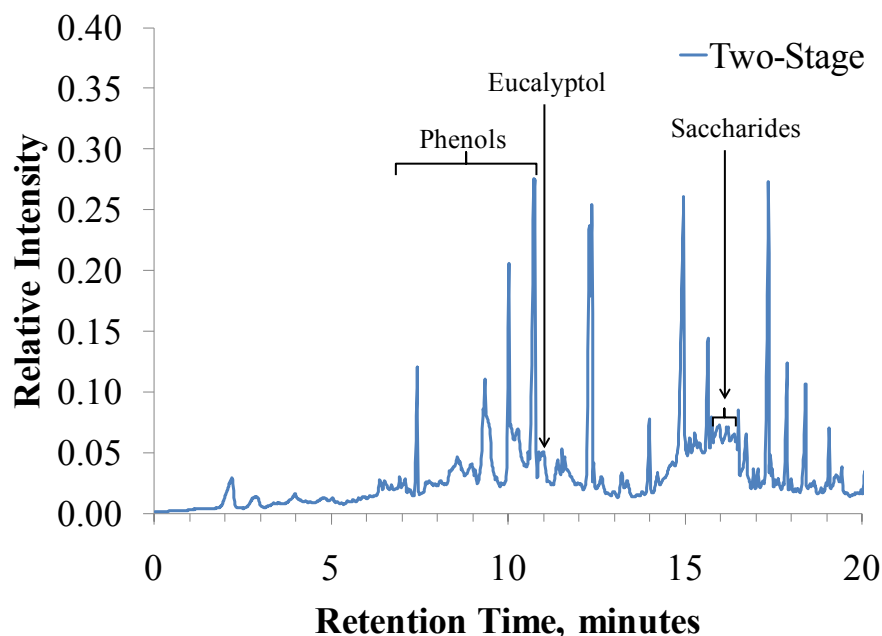

CO2

55% CO_2 Reduction
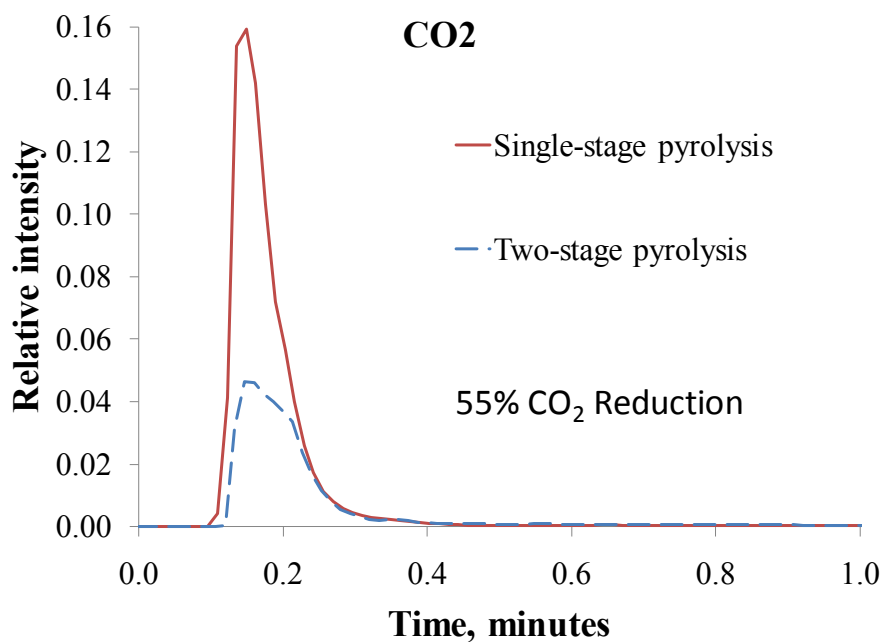
Figure 4.8: Mass spectra transient for carbon dioxide during single-stage and two-stage pyrolysis.

Figure 4.9: **Mass spectra transient for acetic acid during single-stage and two-stage pyrolysis.**

Figure 4.10: Chromatogram for the heavy-weight species from single-stage fast pyrolysis carried out at 600°C.

Figure 4.11: Chromatogram for the heavy-weight species from two-stage fast pyrolysis carried out at 600°C.

4.4 Conclusions

The production of pyrolysis oil presents several challenges including high acidity due to organic acids, high O/C ratios due to light oxygenated species, and high water content. The results in this thesis have shown that using torrefaction as a feedstock pre-treatment method has, at least partly, addressed these issues. When comparing the two stage torrefaction-pyrolysis processing to the single stage processing, a 27% reduction in water and a 67% reduction in acetic acid are observed. In addition, a comparison of the systems' oil fractions displays evidence of reduced light oxygenated species for pyrolysis oil produced from two-stage torrefaction-fast pyrolysis.

5   Overall Conclusions and Recommendations

As research continues to address emerging concerns with renewable energy production, the thermochemical platforms of pyrolysis and torrefaction provide technically challenging, but feasible solutions.   Pyrolysis processing of biomass can produce renewable gas (syngas), and liquid (bio-oil) forms of energy, while torrefaction can produce bio-coal as a premium solid fuel.   The work contained within this thesis was structured around addressing bio-fuels concerns with regards to pyrolysis and torrefaction processing.

Chapter 2 of this thesis addressed fast pyrolysis processing and gasification of forest feedstocks.   From these efforts it was firstly concluded that as temperature increased during gasification, the volume of gas produced increases, the volume of CO_2 decreases and the volumes of CO and CH_4 increase, and the rates of gas evolution increased.   These trends have been documented in the literature, but were confirmed for the forest-based feedstocks studied in this research.   These gaseous formation trends provide mechanistic insights into biomass gasification such that reactions producing carbon monoxide and methane might be favored.   During pyrolysis processing, it was concluded that 30-45% of the original sample mass remained as bio-char in the pyrolysis temperature range of 500 - 700˚C.   The non-char mass was converted to gaseous and vapor products, of which 10-55% is devoted to water and syngas, 2-12% to acetic acid, 2-12% to hydroxypropanone, 1-3% to furaldehyde, and 5-15% to various phenolic compounds.   Research such as this product characterization is highly applied, and only useful if the resulting products can be made technically and economically feasible.

In attempt to address some to the technical feasibility issues the work contained within Chapter 3 and Chapter 4 was performed to address torrefaction and pyrolysis respectively.   In Chapter 3, two mechanistic models were developed to describe species evolution during torrefaction.   Understanding structural changes the biomass undergoes during this treatment can help develop industrial processing methods.   The models proposed are simple, and each have merit in describing the evolution of gaseous and vapor products; describing gaseous product formation as having fast characteristic times

while vapor products such as organic acids have long and delayed evolutions. The two-series reaction model proposes that the parent hemicelluloses material first degrades to a reaction intermediate and some gaseous species, followed by a second reaction where the intermediate further degrades to both gaseous and vapor products. The three-series model adds another reaction, where there is a secondary reaction intermediate which further degrades to gaseous and vapor products. This chapter met the research objective of developing a preliminary model for the production of species during fast torrefaction conditions. The model does, however, need to be refined to possibly include parallel reactions or additional reactions to account for the underprediction of gaseous formation.

The final issue addressed by this thesis is improving the quality of pyrolysis-oil with a novel two stage torrefaction-pyrolysis processing method, described in Chapter 4. Here it was observed that using torrefaction does improve the quality of bio-oil over traditional pyrolysis. Improvements are made by reducing the acidity through organic acid removal, reducing the O/C ratio by removal of some oxygenated species, and removing a portion of the water that would normally reside within the oil. This realization could have important implications, as there are large technical issues with bio-oil due to its instability, and inconsistent storage properties.

As more effort is put forth to advance these challenging renewable energy platforms, it is important to remember that they must also be proven to be socially acceptable and economic solution. So, although it is recommended that these results be further refined and interpreted, it is recommended that the full range of energy sustainability issues be considered, and not simply the technical challenges we face.

Literature Cited

Ayhan D. 2008. Importance of biomass energy sources for Turkey. Energy Policy 36(2):834-842.

Bar-Ziv E, Chudnovsky B. Evaluation of co-firing of raw-biomass and torrefied-biomass with bituminous coals in 575 MW tangentially-fired and 550 MW opposite-wall boilers. Electric Power; 2011; Rosemont, IL.

Bergman PCA. 2005. Combined torrefaction and pelletisation, the TOP process. ECN Biomass, DEN programme of SenterNovem, Dutch Ministry of Economic Affairs, Report ECN-C-05-073.

Bird RB, Stewart WE, Lightfoot EN. 2007. Transport Phenomena. John Wiley & Sons, Inc.

Boardman RD, Hess JR, Sokhansanj S, Tumuluru JS, Wright CT. 2011. A review on biomass torrefaction process and product properties for energy applications. Industrial Biotechnology 7(5):384+.

Bridgwater AV, Meier D, Radlein D. 1999. An overview of fast pyrolysis of biomass. Organic Geochemistry 30(12):1479-1493.

Chen W-H, Hsu H-C, Lu K-M, Lee W-J, Lin T-C. 2011. Thermal pretreatment of wood (Lauan) block by torrefaction and its influence on the properties of the biomass. Energy 36(5):3012-3021.

Chen W-H, Kuo P-C. 2011. Isothermal torrefaction kinetics of hemicellulose, cellulose, lignin and xylan using thermogravimetric analysis. Energy 36(11):6451-6460.

Chew JJ, Doshi V. 2011. Recent advances in biomass pretreatment – Torrefaction fundamentals and technology. Renewable and Sustainable Energy Reviews 15(8):4212-4222.

Ciolkosz D, Wallace R. 2011. A review of torrefaction for bioenergy feedstock production. Biofuels, Bioproducts and Biorefining 5(3):317-329.

Czernik S, Bridgwater AV. 2004. Overview of Applications of Biomass Fast Pyrolysis Oil. Energy & Fuels 18(2):590-598.

Devi L, Ptasinski KJ, Janssen FJJG. 2003. A review of the primary measures for tar elimination in biomass gasification processes. Biomass and Bioenergy 24(2):125-140.

Dizhbite T, Telysheva G, Dobele G, Arshanitsa A, Bikovens O, Andersone A, Kampars V. 2011. Py-GC/MS for characterization of non-hydrolyzed residues from bioethanol production from softwood. Journal of Analytical and Applied Pyrolysis 90(2):126-132.

DOE. 2011. Ethanol market Penetration. US DOE, Alternative Fuels and Advanced Vehicles Data Center.

EIA. 2009. Report #:DOE/EIA-0484, International Energy Outlook, 2009.

EIA. 2010. Annual Energy Projections with Projections to 2035, Report #: DOE/EIA-0383(2010).

EISA. 2007. Energy Independence and Security Act of 2007, Pub. L. No. 110-140.

RTP Overview [Internet]. 2011. [updated 2011, cited 11-25]. Available from: http://www.ensyn.com/technology/overview/

EPA. 2005. Energy Policy Act of 2005, Pub. L. No. 109-58.

Fan J, Kalnes TN, Alward M, Klinger J, Sadehvandi A, Shonnard DR. 2011. Life cycle assessment of electricity generation using fast pyrolysis bio-oil. Renewable Energy 36(2):632-641.

Jackson MA, Compton DL, Boateng AA. 2009. Screening heterogeneous catalysts for the pyrolysis of lignin. Journal of Analytical and Applied Pyrolysis 85(1-2):226-230.

Klinger J, Bar-Ziv E, Shonnard DR. 2011. Personal communication - Torrefaction Experimental Species. Houghton, MI.

Mohan D, Pittman CU, Steele PH. 2006. Pyrolysis of Wood/Biomass for Bio-oil: A Critical Review. Energy & Fuels 20(3):848-889.

NIST. 2011. Chemistry WebBook. National Institute of Standards and Technology. http://webbook.nist.gov/chemistry/.

NREL. 2008. Report NREL/TP-510-42620. National Renewable Energy Laboratory.

Panshin AJ, deZeeuw C. 1980. Textbook of wood technology. New York: McGraw-Hill Book Company.

Patwardhan PR, Satrio JA, Brown RC, Shanks BH. 2009. Product distribution from fast pyrolysis of glucose-based carbohydrates. Journal of Analytical and Applied Pyrolysis 86(2):323-330.

Patwardhan PR, Satrio JA, Brown RC, Shanks BH. 2010. Influence of inorganic salts on the primary pyrolysis products of cellulose. Bioresource Technology 101(12):4646-4655.

Patwardhan PR, Brown RC, Shanks BH. 2011. Product Distribution from the Fast Pyrolysis of Hemicellulose. Sustainable Chemistry & Green Chemistry 4(5):636-643.

Prins MJ, Ptasinski KJ, Janssen FJJG. 2006. Torrefaction of wood: Part 1. Weight loss kinetics. Journal of Analytical and Applied Pyrolysis 77(1):28-34.

Prins MJ, Ptasinski KJ, Janssen FJJG. 2007. From coal to biomass gasification: Comparison of thermodynamic efficiency. Energy 32(7):1248-1259.

REF. 2010. World's largest 'fast pyrolysis' facility to convert biomass into oil. Renewable Energy Focus. Elsevier.

Reichling JP, Kulacki FA. 2011. Comparative analysis of Fischer–Tropsch and integrated gasification combined cycle biomass utilization. Energy 36(11):6529-6535.

Repellin V, Govin A, Rolland M, Guyonnet R. 2010. Modelling anhydrous weight loss of wood chips during torrefaction in a pilot kiln. Biomass and Bioenergy 34(5):602-609.

Spath PL, Mann MK, Kerr DR. 1999. Life Cycle Assessment of Coal-Fired Power Production. NREL/TP-570-25119. Golden, Colorado: National Renewable Energy Laboratory.

van der Stelt MJC, Gerhauser H, Kiel JHA, Ptasinski KJ. 2011. Biomass upgrading by torrefaction for the production of biofuels: A review. Biomass and Bioenergy 35(9):3748-3762.

Yang H, Yan R, Chen H, Lee DH, Zheng C. 2007. Characteristics of hemicellulose, cellulose and lignin pyrolysis. Fuel 86(12-13):1781-1788.

Yat SC, Berger A, Shonnard DR. 2008. Kinetic characterization for dilute sulfuric acid hydrolysis of timber varieties and switchgrass. Bioresource Technology 99(9):3855-3863.

Zhu L, Guo Y, Cheng M, Zhang N, Chen G, Wang Y, Wang Y. 2011. Study on the Methanol Catalytic Synthesis from Biomass Syngas. Advanced Materials Research 347-353:2524-2527.

# Appendix A: Dilute Acid and Enzymatic Hydrolysis of Poplar and Willow

For dilute acid and enzymatic hydrolysis of poplar and willow results, see file "AppxA" located on the supplementary electronic media.

Appendix B: Additional Fast Pyrolysis Product Speciation and Quantification Data

For additional fast pyrolysis product speciation and quantification data, see file "AppxB" located on the supplementary electronic media.

Appendix C: Derivation of Two-Step Series-Reaction Model

$$R_1 \xrightarrow{k_1} R_2 + P_1$$

$$R_2 \xrightarrow{k_2} P_1 + P_2$$
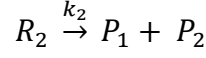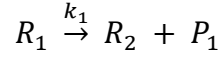
$$k_1 > k_2$$

Summary of Solutions

Reaction Intermediates:

(A) $\dfrac{dR_1}{dt} = -k_1 R_1$ $\qquad\qquad R_1 = (R_1)_o e^{-k_1 t}$

(B) $\dfrac{dR_2}{dt} = k_1 R_1 - k_2 R_2$ $\qquad R_2 = (R_1)_o \dfrac{k_1}{k_1 - k_2}(e^{-k_2 t} - e^{-k_1 t})$

Products:

(C) $\dfrac{dP_1}{dt} = k_1 R_1 + k_2 R_2$ $\qquad \dfrac{dP_1}{dt} = (k_1(R_1)_o - \varepsilon)e^{-k_1 t} + \varepsilon e^{-k_2 t}$

(C) $\dfrac{dP_2}{dt} = k_2 R_2$ $\qquad\qquad \dfrac{dP_2}{dt} = \varepsilon(e^{-k_2 t} - e^{-k_1 t})$

Where:

$$\varepsilon = (R_1)_o \frac{k_1 k_2}{k_1 - k_2}$$

(A) $\dfrac{dR_1}{dt} = -k_1 R_1$

Separate the equation

$$\frac{dR_1}{R_1} = -k_1 dt \tag{1}$$

Integrate (1)

$$\int \frac{1}{R_1} dR_1 = \int -k_1\, dt \tag{2}$$

$$\ln(R_1) = -k_1 t + C_1 \tag{3}$$

$$R_1 = \exp(-k_1 t + C_1) \tag{4}$$

Evaluate (4) at a boundary condition

At $t = 0, R_1 = (R_1)_o, \rightarrow$

$$(R_1)_o = \exp(-k_1(0) + C_1) \tag{5}$$

$$(R_1)_o = \exp(C_1) \tag{6}$$

$$C_1 = \ln((R_1)_o) \tag{7}$$

Replace (7) into (4)

$$R_1 = \exp(-k_1 t + \ln((R_1)_o)) \tag{8}$$

$$R_1 = \exp(-k_1 t)\exp(\ln((R_1)_o))) \tag{9}$$

$$R_1 = (R_1)_o \exp(-k_1 t) \tag{10}$$

$$\boxed{R_1 = (R_1)_o e^{-k_1 t}}$$

(B) $\dfrac{dR_2}{dt} = k_1 R_1 - k_2 R_2$

Previously we found R_1. Replace A(10) into B

$$\frac{dR_2}{dt} = k_1 (R_1)_o \exp(-k_1 t) - k_2 R_2 \tag{1}$$

Assume a simple first order solution for R_2 of the form

$$R_2 = \alpha_1 \exp(-k_1 t) + \alpha_2 \exp(-k_2 t) \tag{2}$$

Replace (2) into (1)

$$\frac{dR_2}{dt} = k_1 (R_1)_o \exp(-k_1 t) - k_2 (\alpha_1 \exp(-k_1 t) + \alpha_2 \exp(-k_2 t)) \tag{3}$$

Now also consider the time derivative of (2)

$$\frac{dR_2}{dt} = -k_1 \alpha_1 \exp(-k_1 t) - k_2 \alpha_2 \exp(-k_2 t) \tag{4}$$

Rearrange (3) to more convenient form

$$\frac{dR_2}{dt} = (k_1 (R_1)_o - k_2 \alpha_1) \exp(-k_1 t) - k_2 \alpha_2 \exp(-k_2 t) \tag{5}$$

Comparing (4) and (5) we can find α_1 for the assumed solution

$$-k_1 \alpha_1 = k_1 (R_1)_o - k_2 \alpha_1 \tag{6}$$

$$-k_1 \alpha_1 + k_2 \alpha_1 = k_1 (R_1)_o \tag{7}$$

$$\alpha_1 = \frac{k_1}{k_2 - k_1} (R_1)_o \tag{8}$$

Evaluating (2) at a boundary condition

At $t = 0, R_2 = 0, \rightarrow$

$$0 = \alpha_1 \exp(-k_1 0) + \alpha_2 \exp(-k_2 0) \tag{9}$$

$$\alpha_1 = -\alpha_2 \tag{10}$$

Replacing (8) into (2) and using the relationship in (10)

$$R_2 = \frac{k_1}{k_2 - k_1} (R_1)_o \exp(-k_1 t) - \frac{k_1}{k_2 - k_1} (R_1)_o \exp(-k_2 t) \tag{11}$$

$$R_2 = \frac{k_1}{k_2 - k_1} (R_1)_o (\exp(-k_1 t) - \exp(-k_2 t)) \tag{12}$$

Noting that $k_1 > k_2 > k_3$, rearrange expression

$$R_2 = \frac{k_1}{k_1 - k_2}(R_1)_o(\exp(-k_2t) - \exp(-k_1t)) \tag{13}$$

$$\boxed{R_2 = \frac{k_1}{k_1 - k_2}(R_1)_o(e^{-k_2t} - e^{-k_1t})}$$

(C) $\dfrac{dP_1}{dt} = k_1R_1 + k_2R_2$

Previously we found R_1 and R_2. Replace A(10) and B(13) into C

$$\frac{dP_1}{dt} = k_1(R_1)_oe^{-k_1t} + k_2\frac{k_1}{k_1 - k_2}(R_1)_o(e^{-k_2t} - e^{-k_1t}) \tag{1}$$

$$\frac{dP_1}{dt} = k_1(R_1)_oe^{-k_1t} + \frac{k_1k_2(R_1)_o}{k_1 - k_2}e^{-k_2t} - \frac{k_1k_2(R_1)_o}{k_1 - k_2}e^{-k_1t} \tag{2}$$

$$\frac{dP_1}{dt} = \left(k_1(R_1)_o - \frac{k_1k_2(R_1)_o}{k_1 - k_2}\right)e^{-k_1t} + \frac{k_1k_2(R_1)_o}{k_1 - k_2}e^{-k_2t} \tag{3}$$

$$\frac{dP_1}{dt} = k_1(R_1)_o\left(\left(1 - \frac{k_2}{k_1 - k_2}\right)e^{-k_1t} + \frac{k_2}{k_1 - k_2}e^{-k_2t}\right) \tag{4}$$

$$\boxed{\frac{dP_1}{dt} = k_1(R_1)_o\left(\left(1 - \frac{k_2}{k_1 - k_2}\right)e^{-k_1t} + \frac{k_2}{k_1 - k_2}e^{-k_2t}\right)}$$

(D) $\dfrac{dP_2}{dt} = k_2 R_2$

Previously we found R_2. Replace B(13) into D

$$\frac{dP_2}{dt} = k_2 \frac{k_1}{k_1 - k_2} (R_1)_o (e^{-k_2 t} - e^{-k_1 t}) \tag{1}$$

$$\boxed{\frac{dP_2}{dt} = k_1 (R_1)_o \frac{k_2}{k_1 - k_2} (e^{-k_2 t} - e^{-k_1 t})}$$

It would simplify the equations and make relationships more apparent to define a constants that substitutes for others. C(4) and D(1) would then respectively become
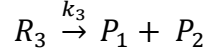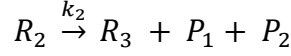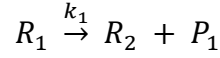
$$\frac{dP_1}{dt} = (k_1 (R_1)_o - \varepsilon) e^{-k_1 t} + \varepsilon e^{-k_2 t}$$

$$\frac{dP_2}{dt} = \varepsilon (e^{-k_2 t} - e^{-k_1 t})$$

Where:

$$\varepsilon = (R_1)_o \frac{k_1 k_2}{k_1 - k_2}$$

Appendix D: Derivation of Three-Step Series-Reaction Model

$$R_1 \xrightarrow{k_1} R_2 + P_1$$

$$R_2 \xrightarrow{k_2} R_3 + P_1 + P_2$$

$$R_3 \xrightarrow{k_3} P_1 + P_2$$

$$k_1 > k_2 > k_3$$

Summary of Solutions

Reaction Intermediates:

(A) $\dfrac{dR_1}{dt} = -k_1 R_1$ $\qquad R_1 = (R_1)_o e^{-k_1 t}$

(B) $\dfrac{dR_2}{dt} = k_1 R_1 - k_2 R_2$ $\qquad R_2 = (R_1)_o \dfrac{k_1}{k_1 - k_2}(e^{-k_2 t} - e^{-k_1 t})$

(C) $\dfrac{dR_3}{dt} = k_2 R_2 - k_3 R_3$ $\qquad \begin{aligned} R_3 = \delta(R_1)_o[&(k_2 - k_3)(e^{-k_1 t} - e^{-k_3 t}) \\ &+ (k_1 - k_3)(e^{-k_3 t} - e^{-k_2 t})] \end{aligned}$

Products:

(D) $\dfrac{dP_1}{dt} = k_1 R_1 + k_2 R_2 + k_3 R_3$ $\qquad \dfrac{1}{(R_1)_o}\dfrac{dP_1}{dt} = (k_1 + \alpha)e^{-k_1 t} + \beta e^{-k_2 t} + \gamma e^{-k_3 t}$

(E) $\dfrac{dP_2}{dt} = k_2 R_2 + k_3 R_3$ $\qquad \dfrac{1}{(R_1)_o}\dfrac{dP_2}{dt} = \alpha e^{-k_1 t} + \beta e^{-k_2 t} + \gamma e^{-k_3 t}$

Where:

$$\alpha = \dfrac{k_1 k_2 k_3}{(k_1 - k_2)(k_1 - k_3)} - \dfrac{k_1 k_2}{k_1 - k_2}$$

$$\beta = \dfrac{k_1 k_2}{k_1 - k_2} - \dfrac{k_1 k_2 k_3}{(k_1 - k_2)(k_2 - k_3)}$$

$$\gamma = \dfrac{k_1 k_2 k_3}{(k_1 - k_2)(k_2 - k_3)} - \dfrac{k_1 k_2 k_3}{(k_1 - k_2)(k_1 - k_3)}$$

$$\delta = \dfrac{k_1 k_2}{(k_1 - k_2)(k_1 - k_3)(k_2 - k_3)}$$

73

With the previous model, expressions were found for (A) and (B), continuing with the solutions found above,

(C) $\dfrac{dR_3}{dt} = k_2 R_2 - k_3 R_3$

Previously we found R_2. Replace B(13) into C

$$\frac{dR_3}{dt} = k_2 \left(\frac{k_1}{k_1 - k_2} (R_1)_o (e^{-k_2 t} - e^{-k_1 t}) \right) - k_3 R_3 \tag{1}$$

Assume a simple first order solution for R_3 of the form

$$R_3 = \alpha_1 e^{-k_1 t} + \alpha_2 e^{-k_2 t} + \alpha_3 e^{-k_3 t} \tag{2}$$

Replace (2) into (1)

$$\frac{dR_3}{dt} = k_2 \left(\frac{k_1}{k_1 - k_2} (R_1)_o (e^{-k_2 t} - e^{-k_1 t}) \right)$$
$$- k_3 (\alpha_1 e^{-k_1 t} + \alpha_2 e^{-k_2 t} + \alpha_3 e^{-k_3 t}) \tag{3}$$

Now also consider the time derivative of (2)

$$\frac{dR_3}{dt} = -k_1 \alpha_1 \exp(-k_1 t) - k_2 \alpha_2 \exp(-k_2 t) - k_3 \alpha_3 \exp(-k_3 t) \tag{4}$$

Rearrange (3) to more convenient form

$$\frac{dR_3}{dt} = k_2 \frac{k_1}{k_1 - k_2} (R_1)_o e^{-k_2 t} - k_2 \frac{k_1}{k_1 - k_2} (R_1)_o e^{-k_1 t} - k_3 \alpha_1 e^{-k_1 t}$$
$$- k_3 \alpha_2 e^{-k_2 t} - k_3 \alpha_3 e^{-k_3 t} \tag{5}$$

$$\frac{dR_3}{dt} = \left(-\frac{k_1 k_2}{k_1 - k_2} (R_1)_o - k_3 \alpha_1 \right) e^{-k_1 t}$$
$$+ \left(\frac{k_1 k_2}{k_1 - k_2} (R_1)_o - k_3 \alpha_2 \right) e^{-k_2 t} - k_3 \alpha_3 e^{-k_3 t} \tag{6}$$

Comparing (4) and (6) we can find α_1 and α_2 for the assumed solution

$$-k_1 \alpha_1 = -\frac{k_1 k_2}{k_1 - k_2} (R_1)_o - k_3 \alpha_1 \tag{7}$$

$$-k_1 \alpha_1 + k_3 \alpha_1 = -\frac{k_1 k_2}{k_1 - k_2} (R_1)_o \tag{8}$$

$$\alpha_1 = -\frac{k_2}{k_3 - k_1} \frac{k_1}{k_1 - k_2} (R_1)_o \tag{9}$$

74

$$-k_2\alpha_2 = \frac{k_1 k_2}{k_1 - k_2}(R_1)_o - k_3\alpha_2 \tag{10}$$

$$-k_2\alpha_2 + k_3\alpha_2 = \frac{k_1 k_2}{k_1 - k_2}(R_1)_o \tag{11}$$

$$\alpha_2 = \frac{k_2}{k_3 - k_2}\frac{k_1}{k_1 - k_2}(R_1)_o \tag{12}$$

Evaluating (2) at a boundary condition

At $t = 0, R_3 = 0, \rightarrow$

$$0 = \alpha_1 \exp(-k_1 0) + \alpha_2 \exp(-k_2 0) + \alpha_3 \exp(-k_3 0) \tag{14}$$

$$\alpha_3 = -\alpha_1 - \alpha_2 \tag{15}$$

Replacing (9) and (12) into (2) and using the relationship in (15)

$$R_3 = \overbrace{\frac{k_2}{k_1 - k_3}\frac{k_1}{k_1 - k_2}(R_1)_o}^{\alpha 1} e^{-k_1 t} - \overbrace{\frac{k_2}{k_2 - k_3}\frac{k_1}{k_1 - k_2}(R_1)_o}^{\alpha 2} e^{-k_2 t}$$
$$+ \overbrace{\left(\frac{k_2}{k_2 - k_3} - \frac{k_2}{k_1 - k_3}\right)\frac{k_1}{k_1 - k_2}(R_1)_o}^{\alpha 3} e^{-k_3 t} \tag{16}$$

Simplify

$$R_3 = \frac{k_1}{k_1 - k_2}(R_1)_o \left(\frac{k_2}{k_1 - k_3}\exp(-k_1 t) - \frac{k_2}{k_2 - k_3}\exp(-k_2 t)\right.$$
$$\left.+ \left(\frac{k_2}{k_2 - k_3} - \frac{k_2}{k_1 - k_3}\right)\exp(-k_3 t)\right) \tag{17}$$

$$R_3 = \frac{k_1}{k_1 - k_2}(R_1)_o \left(\frac{k_2(k_2 - k_3)}{(k_1 - k_3)(k_2 - k_3)}\exp(-k_1 t)\right.$$
$$- \frac{k_2(k_1 - k_3)}{(k_2 - k_3)(k_1 - k_3)}\exp(-k_2 t)$$
$$+ \left(\frac{k_2(k_1 - k_3)}{(k_2 - k_3)(k_1 - k_3)}\right.$$
$$\left.\left.- \frac{k_2(k_2 - k_3)}{(k_1 - k_3)(k_2 - k_3)}\right)\exp(-k_3 t)\right) \tag{18}$$

$$R_3 = \frac{k_1}{k_1 - k_2}(R_1)_o \left(\frac{k_2(k_2 - k_3)}{(k_1 - k_3)(k_2 - k_3)} \exp(-k_1 t) \right.$$

$$- \frac{k_2(k_1 - k_3)}{(k_2 - k_3)(k_1 - k_3)} \exp(-k_2 t)$$

$$+ \frac{k_2(k_1 - k_3)}{(k_2 - k_3)(k_1 - k_3)} \exp(-k_3 t)$$

$$\left. - \frac{k_2(k_2 - k_3)}{(k_1 - k_3)(k_2 - k_3)} \exp(-k_3 t) \right)$$

(19)

$$R_3 = \frac{k_1}{k_1 - k_2}(R_1)_o \frac{1}{(k_1 - k_3)(k_2 - k_3)}(k_2(k_2 - k_3)\exp(-k_1 t)$$

$$- k_2(k_1 - k_3)\exp(-k_2 t) + k_2(k_1 - k_3)\exp(-k_3 t)$$

$$- k_2(k_2 - k_3)\exp(-k_3 t))$$

(20)

$$R_3 = \frac{k_1}{(k_1 - k_2)(k_1 - k_3)(k_2 - k_3)}(R_1)_o(k_2(k_2 - k_3)\exp(-k_1 t)$$

$$- k_2(k_1 - k_3)\exp(-k_2 t) + k_2(k_1 - k_3)\exp(-k_3 t)$$

$$- k_2(k_2 - k_3)\exp(-k_3 t))$$

(21)

$$R_3 = \frac{k_1 k_2}{(k_1 - k_2)(k_1 - k_3)(k_2 - k_3)}(R_1)_o[(k_2 - k_3)(\exp(-k_1 t)$$

$$- \exp(-k_3 t)) + (k_1 - k_3)(\exp(-k_3 t) - \exp(-k_2 t))]$$

(22)

$$\boxed{\begin{array}{c} R_3 = \dfrac{k_1 k_2}{(k_1 - k_2)(k_1 - k_3)(k_2 - k_3)}(R_1)_o[(k_2 - k_3)(e^{-k_1 t} - e^{-k_3 t}) \\ + (k_1 - k_3)(e^{-k_3 t} - e^{-k_2 t})] \end{array}}$$

(D) $\dfrac{dP_1}{dt} = k_1R_1 + k_2R_2 + k_3R_3$

Previously we found R_1, R_2, R_3. Replace A(10), B(13), and C(22) into D

$\dfrac{dP_1}{dt}$

$$= k_1 \overbrace{(R_1)_o e^{-k_1 t}}^{R_1} + k_2 \overbrace{\dfrac{k_1}{k_1 - k_2} (R_1)_o (e^{-k_2 t} - e^{-k_1 t})}^{R_2}$$

$$+ k_3 \overbrace{\dfrac{k_1 k_2}{(k_1 - k_2)(k_1 - k_3)(k_2 - k_3)} (R_1)_o}^{R_3} \tag{1}$$

$$* \overbrace{[(k_2 - k_3)(e^{-k_1 t} - e^{-k_3 t}) + (k_1 - k_3)(e^{-k_3 t} - e^{-k_2 t})]}^{R_3}$$

$\dfrac{1}{(R_1)_o} \dfrac{dP_1}{dt}$

$$= k_1 e^{-k_1 t} + k_2 \dfrac{k_1}{k_1 - k_2} (e^{-k_2 t} - e^{-k_1 t})$$

$$+ k_3 \dfrac{k_1 k_2}{(k_1 - k_2)(k_1 - k_3)(k_2 - k_3)} [(k_2 - k_3)(e^{-k_1 t} \tag{2}$$

$$- e^{-k_3 t}) + (k_1 - k_3)(e^{-k_3 t} - e^{-k_2 t})]$$

$\dfrac{1}{(R_1)_o} \dfrac{dP_1}{dt}$

$$= k_1 e^{-k_1 t} + k_2 \dfrac{k_1}{k_1 - k_2} e^{-k_2 t} - k_2 \dfrac{k_1}{k_1 - k_2} e^{-k_1 t}$$

$$+ k_3 \dfrac{k_1 k_2}{(k_1 - k_2)(k_1 - k_3)(k_2 - k_3)} (k_2 - k_3)(e^{-k_1 t} \tag{3}$$

$$- e^{-k_3 t})$$

$$+ k_3 \dfrac{k_1 k_2}{(k_1 - k_2)(k_1 - k_3)(k_2 - k_3)} (k_1 - k_3)(e^{-k_3 t}$$

$$- e^{-k_2 t})$$

$$\frac{1}{(R_1)_o}\frac{dP_1}{dt}$$

$$= k_1 e^{-k_1 t} + k_2 \frac{k_1}{k_1 - k_2} e^{-k_2 t} - k_2 \frac{k_1}{k_1 - k_2} e^{-k_1 t}$$

$$+ k_3 \frac{k_1 k_2 (k_2 - k_3)}{(k_1 - k_2)(k_1 - k_3)(k_2 - k_3)} e^{-k_1 t}$$

$$- k_3 \frac{k_1 k_2 (k_2 - k_3)}{(k_1 - k_2)(k_1 - k_3)(k_2 - k_3)} e^{-k_3 t} \qquad (4)$$

$$+ k_3 \frac{k_1 k_2 (k_1 - k_3)}{(k_1 - k_2)(k_1 - k_3)(k_2 - k_3)} e^{-k_3 t}$$

$$- k_3 \frac{k_1 k_2 (k_1 - k_3)}{(k_1 - k_2)(k_1 - k_3)(k_2 - k_3)} e^{-k_2 t}$$

$$\frac{1}{(R_1)_o}\frac{dP_1}{dt}$$

$$= \left(k_1 + k_3 \frac{k_1 k_2 (k_2 - k_3)}{(k_1 - k_2)(k_1 - k_3)(k_2 - k_3)} \right.$$

$$\left. - k_2 \frac{k_1}{k_1 - k_2} \right) e^{-k_1 t}$$

$$+ \left(k_2 \frac{k_1}{k_1 - k_2} \right. \qquad (5)$$

$$\left. - k_3 \frac{k_1 k_2 (k_1 - k_3)}{(k_1 - k_2)(k_1 - k_3)(k_2 - k_3)} \right) e^{-k_2 t}$$

$$+ \left(k_3 \frac{k_1 k_2 (k_1 - k_3)}{(k_1 - k_2)(k_1 - k_3)(k_2 - k_3)} \right.$$

$$\left. - k_3 \frac{k_1 k_2 (k_2 - k_3)}{(k_1 - k_2)(k_1 - k_3)(k_2 - k_3)} \right) e^{-k_3 t}$$

$$\frac{1}{(R_1)_o}\frac{dP_1}{dt}$$

$$= \left(k_1 + k_3\frac{k_1k_2}{(k_1-k_2)(k_1-k_3)} - k_2\frac{k_1}{k_1-k_2}\right)e^{-k_1t}$$

$$+ \left(k_2\frac{k_1}{k_1-k_2} - k_3\frac{k_1k_2}{(k_1-k_2)(k_2-k_3)}\right)e^{-k_2t} \qquad (6)$$

$$+ \left(k_3\frac{k_1k_2}{(k_1-k_2)(k_2-k_3)}\right.$$

$$\left. - k_3\frac{k_1k_2}{(k_1-k_2)(k_1-k_3)}\right)e^{-k_3t}$$

$$\boxed{\begin{aligned}\frac{1}{(R_1)_o}\frac{dP_1}{dt} &= \left(k_1 + \frac{k_1k_2k_3}{(k_1-k_2)(k_1-k_3)} - \frac{k_1k_2}{k_1-k_2}\right)e^{-k_1t}\\ &+ \left(\frac{k_1k_2}{k_1-k_2} - \frac{k_1k_2k_3}{(k_1-k_2)(k_2-k_3)}\right)e^{-k_2t}\\ &+ \left(\frac{k_1k_2k_3}{(k_1-k_2)(k_2-k_3)} - \frac{k_1k_2k_3}{(k_1-k_2)(k_1-k_3)}\right)e^{-k_3t}\end{aligned}}$$

(E) $\quad \dfrac{dP_2}{dt} = k_2R_2 + k_3R_3$

Previously we found R_2, R_3. Replace B(13) and C(22) into E

$$\frac{dP_2}{dt} = k_2\frac{k_1}{k_1-k_2}(R_1)_o(e^{-k_2t} - e^{-k_1t})$$

$$+ k_3\frac{k_1k_2}{(k_1-k_2)(k_1-k_3)(k_2-k_3)}(R_1)_o[(k_2 \qquad (1)$$

$$- k_3)(e^{-k_1t} - e^{-k_3t}) + (k_1 - k_3)(e^{-k_3t} - e^{-k_2t})]$$

$$\frac{1}{(R_1)_o}\frac{dP_2}{dt}$$

$$= k_2 \frac{k_1}{k_1 - k_2}(e^{-k_2 t} - e^{-k_1 t}) \tag{2}$$

$$+ k_3 \frac{k_1 k_2}{(k_1 - k_2)(k_1 - k_3)(k_2 - k_3)}[(k_2 - k_3)(e^{-k_1 t} - e^{-k_3 t}) + (k_1 - k_3)(e^{-k_3 t} - e^{-k_2 t})]$$

$$\frac{1}{(R_1)_o}\frac{dP_2}{dt}$$

$$= k_2 \frac{k_1}{k_1 - k_2}(e^{-k_2 t} - e^{-k_1 t})$$

$$+ k_3 \frac{k_1 k_2 (k_2 - k_3)}{(k_1 - k_2)(k_1 - k_3)(k_2 - k_3)} e^{-k_1 t}$$

$$- k_3 \frac{k_1 k_2 (k_2 - k_3)}{(k_1 - k_2)(k_1 - k_3)(k_2 - k_3)} e^{-k_3 t} \tag{3}$$

$$+ k_3 \frac{k_1 k_2 (k_1 - k_3)}{(k_1 - k_2)(k_1 - k_3)(k_2 - k_3)} e^{-k_3 t}$$

$$- k_3 \frac{k_1 k_2 (k_1 - k_3)}{(k_1 - k_2)(k_1 - k_3)(k_2 - k_3)} e^{-k_2 t}$$

$$\frac{1}{(R_1)_o}\frac{dP_2}{dt}$$

$$= \left(k_3 \frac{k_1 k_2 (k_2 - k_3)}{(k_1 - k_2)(k_1 - k_3)(k_2 - k_3)} \right.$$

$$\left. - k_2 \frac{k_1}{k_1 - k_2} \right) e^{-k_1 t}$$

$$+ \left(k_2 \frac{k_1}{k_1 - k_2} \right.$$

$$\left. - k_3 \frac{k_1 k_2 (k_1 - k_3)}{(k_1 - k_2)(k_1 - k_3)(k_2 - k_3)} \right) e^{-k_2 t} \tag{4}$$

$$+ \left(k_3 \frac{k_1 k_2 (k_1 - k_3)}{(k_1 - k_2)(k_1 - k_3)(k_2 - k_3)} \right.$$

$$\left. - k_3 \frac{k_1 k_2 (k_2 - k_3)}{(k_1 - k_2)(k_1 - k_3)(k_2 - k_3)} \right) e^{-k_3 t}$$

$$\frac{1}{(R_1)_o}\frac{dP_2}{dt} = \left(\frac{k_1 k_2 k_3}{(k_1 - k_2)(k_1 - k_3)} - \frac{k_1 k_2}{k_1 - k_2}\right)e^{-k_1 t}$$

$$+ \left(\frac{k_1 k_2}{k_1 - k_2} - \frac{k_1 k_2 k_3}{(k_1 - k_2)(k_2 - k_3)}\right)e^{-k_2 t}$$

$$+ \left(\frac{k_1 k_2 k_3}{(k_1 - k_2)(k_2 - k_3)} - \frac{k_1 k_2 k_3}{(k_1 - k_2)(k_1 - k_3)}\right)e^{-k_3 t}$$

Noting the similarities between D(6) and E(4), it would greatly simplify the equations to define several constants that are calculated from relationships between the rate constants. D(6) and E(4) would then respectively become

$$\frac{1}{(R_1)_o}\frac{dP_1}{dt} = (k_1 + \alpha)e^{-k_1 t} + \beta e^{-k_2 t} + \gamma e^{-k_3 t}$$

$$\frac{1}{(R_1)_o}\frac{dP_2}{dt} = \alpha e^{-k_1 t} + \beta e^{-k_2 t} + \gamma e^{-k_3 t}$$

Where:

$$\alpha = \frac{k_1 k_2 k_3}{(k_1 - k_2)(k_1 - k_3)} - \frac{k_1 k_2}{k_1 - k_2}$$

$$\beta = \frac{k_1 k_2}{k_1 - k_2} - \frac{k_1 k_2 k_3}{(k_1 - k_2)(k_2 - k_3)}$$

$$\gamma = \frac{k_1 k_2 k_3}{(k_1 - k_2)(k_2 - k_3)} - \frac{k_1 k_2 k_3}{(k_1 - k_2)(k_1 - k_3)}$$

Appendix E: Taylor Dispersion Comparison of Pulse-Response

To use the generalized Taylor dispersion models presented in Bird, Stewart, and Lightfoots text(Bird et al. 2007), a value for diffusion coefficient first had to be obtained. The equation used for estimating the this coefficient was the Wilke-Change Equation, Equation (17.4-8) presented on page 530 of the text(Bird et al. 2007). The expression is empirically based and is valid for small concentrations of A in B:

$$D_{AB} = 7.4 \times 10^{-8} \frac{\sqrt{\varphi_B M_B T}}{\mu \tilde{V}_A^{0.6}}$$

where D_{AB} is the diffusion coefficient in cm^2/sec, φ_B is an association parameter (1.0 for unassociated solvents), M_B is the molecular weight of B, T is the absolute temperature in K, μ is the viscosity in cP, and $\tilde{V}_A$ is the molar volume of species A in cm^3/mol (Bird et al. 2007).

Using properties of helium and carbon dioxide at ambient conditions, the diffusivity coefficient was found to be 5.636×10^{-6} cm^2/sec. The axial dispersion coefficient was then found using Equation (20.5-15) on page 645 of the text(Bird et al. 2007):

$$K = \frac{R^2 \langle v_z \rangle^2}{48 D_{AB}}$$

where R is the radius in cm, $\langle v_z \rangle$ is the average velocity through the column in cm/s, and K is the dispersion coefficient in cm^2/sec. The "best estimate" dispersion coefficient was found to be 1,498 cm^2/sec. The concentration profile solution is presented as Equation (20.5-18) on page 645 of the text(Bird et al. 2007):

$$\langle \rho_A \rangle = \frac{m_A}{2\pi R^2 \sqrt{\pi K t}} \exp\left(-\frac{(z - \langle v_z \rangle t)^2}{4Kt}\right)$$

where m_A is a mass input of A, t is time in seconds, and z is the length coordinate in cm(Bird et al. 2007). When this equation is solved at the exit (z = 3000 cm), the solution

shown in Figure 29 is obtained. One half, and two times the axial dispersion coefficient values were also considered to interpret sensitivity. Figure 5.2 shows the results from the CO_2 input-response (time shifted such that input occurs at t=0) with the best estimate axial dispersion solution.

From these results, it is clear that there are other factors that further delay the response of the instrument, such as the pyrolysis instrument transfer line. In addition, the measured response is much narrower that the predicted solution. The reason for this is unclear, but may be due to an overestimate in the value of the axial dispersion coefficient, K, which would lead to an underestimate in the diffusivity coefficient, D_{AB}. There general solutions for dispersion are symmetrical, whereas the response curve has a slower decrease in signal. In summary Taylor dispersion cannot fully explain the dynamics of the CO_2 flow system, and it is clear that there are other factors affecting the observed signal response.
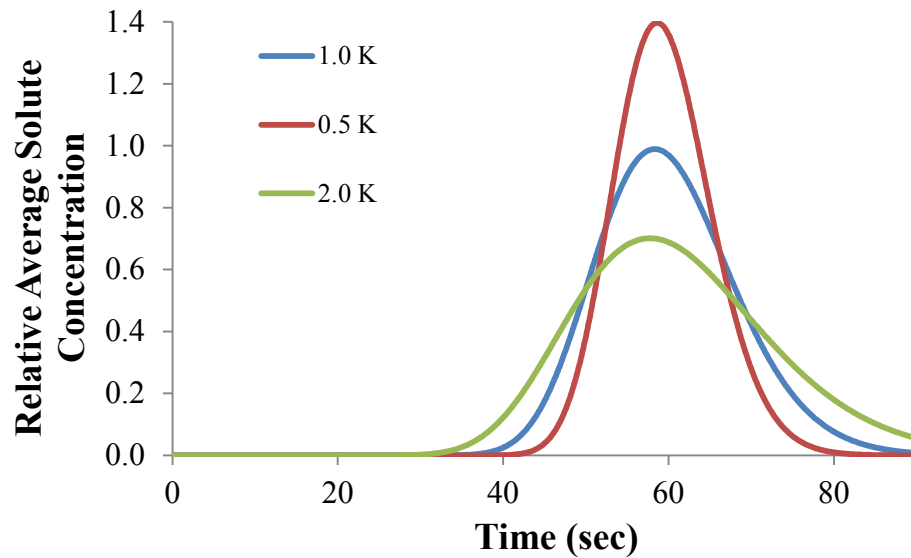
Figure 5.1: Exit concentration from Taylor dispersions solutions for CO_2 in He at low concentration and laminar flow
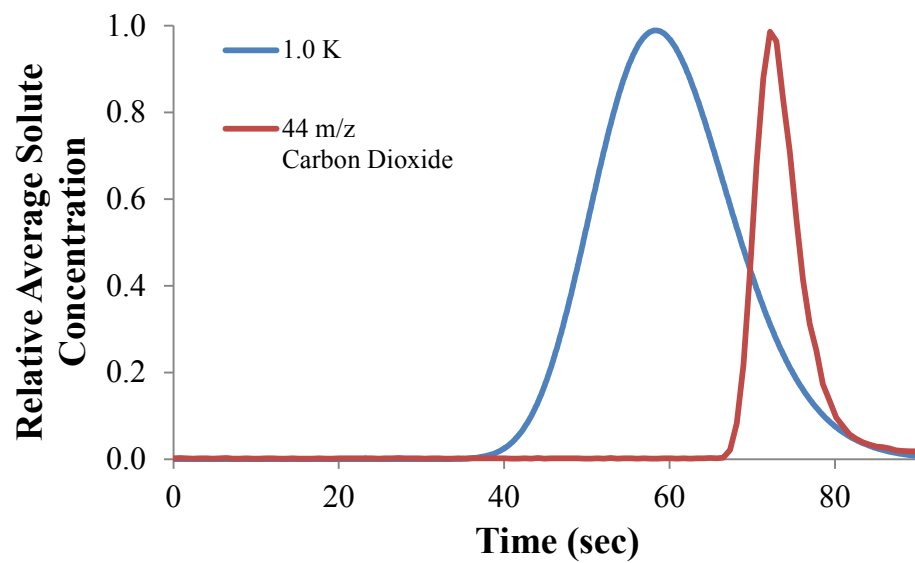
Figure 5.2: General Taylor dispersion solution compared to CO$_2$ pulse experiment